

CONSTRAINING GLOBAL PROPERTIES OF THE DRACO DWARF SPHEROIDAL GALAXY

SERGEY MASHCHENKO, ALISON SILLS, AND H. M. COUCHMAN

Department of Physics and Astronomy, McMaster University, Hamilton, ON, L8S 4M1, Canada;
 syam@physics.mcmaster.ca, couchman@physics.mcmaster.ca, asills@physics.mcmaster.ca

Received 2005 September 22; accepted 2005 November 18

ABSTRACT

By fitting a flexible stellar anisotropy model to the observed surface brightness and line-of-sight velocity dispersion profiles of Draco we derive a sequence of cosmologically plausible two-component (stars + dark matter) models for this galaxy. The models are consistent with all the available observations and can have either cuspy Navarro-Frenk-White or flat-cored dark matter density profiles. The dark matter halos either formed relatively recently (at $z \sim 2-7$) and are massive (up to $\sim 5 \times 10^9 M_\odot$), or formed before the end of the reionization of the universe ($z \sim 7-11$) and are less massive (down to $\sim 7 \times 10^7 M_\odot$). Our results thus support either of the two popular solutions of the “missing satellites” problem of Λ cold dark matter cosmology—that dwarf spheroidals are either very massive or very old. We carry out high-resolution simulations of the tidal evolution of our two-component Draco models in the potential of the Milky Way. The results of our simulations suggest that the observable properties of Draco have not been appreciably affected by the Galactic tides after 10 Gyr of evolution. We rule out Draco being a “tidal dwarf”—a tidally disrupted dwarf galaxy. Almost radial Draco orbits (with the pericentric distance $\lesssim 15$ kpc) are also ruled out by our analysis. The case of a harmonic dark matter core can be consistent with observations only for a very limited choice of Draco orbits (with the apocentric-to-pericentric distances ratio of $\lesssim 2.5$).

Subject headings: galaxies: evolution — galaxies: individual (Draco dwarf spheroidal) — stellar dynamics

1. INTRODUCTION

Galactic dwarf spheroidal galaxies (dSphs) are intriguing objects with a deceptively simple appearance—roughly spheroidal shape, no gas, and no recent star formation. Due to their closeness, these galaxies are studied in significantly more detail than other external galaxies (see the review of Mateo 1998). Despite that, the nature of dSphs and their place in the larger cosmological picture is not well understood.

The first wave of enhanced interest in dSphs took off after the pioneer work of Aaronson (1983). Based only on the three stars in Draco with measured line-of-sight velocities, he boldly claimed that Draco can be significantly dark matter (DM) dominated. The fact that the stellar velocity dispersion in dSphs is significantly larger than what would follow from the virial theorem for the luminous mass was later confirmed with much larger studies. For example, the latest compilation of Wilkinson et al. (2004) contained 207 Draco stars with measured line-of-sight velocities. Similar results were obtained for other dSphs as well—both for the Milky Way and M31 satellites. There were attempts to explain the large stellar velocity dispersion in Galactic dSphs without invoking the DM hypothesis. Most notably, Kroupa (1997) presented a model where dSphs are considered to be “tidal dwarfs”—virtually unbound stellar streams from dwarf galaxies tidally disrupted in the Milky Way potential. The model of Kroupa (1997) appears to be not applicable to Draco as it is unable to reproduce the narrow observed horizontal branch width of this dwarf (Klessen et al. 2003). In this paper we present additional evidence against Draco being a tidal dwarf. The overall consensus now appears to be that dSphs do contain significant amounts of DM and are hence the smallest known objects with (indirectly) detected DM. This makes them very interesting objects, as they can be an important test bench for modern cosmological models and for the theories of DM.

More recently, the interest in dSphs was rejuvenated after the realization that simple (DM-only) cosmological models over-

predict the number of the Milky Way satellite galaxies by 1–2 orders of magnitude (Klypin et al. 1999; Moore et al. 1999). This was coined the “missing satellite problem” of cosmology. The original analysis was done under the assumption that DM in dSphs has the same spatial extent as stars. Relaxation of the above assumption led to a suggestion that only the most massive subhalos predicted to populate a Galaxy-sized halo managed to form stars, with the rest of the subhalos staying dark (Stoeckl et al. 2002). Another way of solving the missing satellites problem is to assume that only the oldest subhalos formed stars, with the star formation in the younger subhalos being suppressed by the metagalactic ionizing radiation after the reionization of the universe was accomplished around $z \sim 6.5$ (Bullock et al. 2000). In reality, both mechanisms could have realized (Ricotti & Gnedin 2005).

To discriminate between the two above solutions of the missing satellites problem and to place Galactic dSphs in the right cosmological context one has to know the global parameters of these dwarfs, and most importantly, their total DM extent and mass. The traditional approach is to assume that the dwarf is in equilibrium (thus ignoring the possible impact of the Galactic tides), and to solve the Jeans equation to infer the density profile of the DM halo based on the observed surface brightness and line-of-sight velocity dispersion profiles. As the proper motions of individual stars in dSphs are not known, one has to resort to making certain assumptions about the anisotropy in the stellar velocities. Due to a well-known degeneracy between the assumed stellar anisotropy and inferred total enclosed mass there are many solutions to the Jeans equation that are consistent with the observations. Another limitation of the above approach is that DM can be traced only within the stellar body extent of the dwarf, so no conclusion can be made about the total mass of the galaxy. It is also not clear at what distance from the dwarf’s center the virial equilibrium assumption breaks down due to Galactic tides. Some work has been done on the impact of tidal forces on the structure of Galactic satellites (e.g., Oh et al. 1995; Piatek & Pryor 1995; Hayashi et al. 2003; Kazantzidis et al. 2004), where it was clearly demonstrated

that the tidal stripping and shocking is a complex dynamic process. The deficiency of the above work is in using single-component models for the dwarf galaxies, which made it impossible to directly compare the results of the numerical simulations with the observations. In general, stars in dSphs are distributed differently from DM, so they also behave differently in reaction to the external tides. To correctly describe the observable manifestations of the Galactic tides in dSphs it is essential to use two-component (stars + DM) dwarf models (Read et al. 2006).

In this paper we place joint constraints on the global properties of Draco (one of the best studied dSphs) by (1) using cosmological predictions for the properties of DM halos, (2) developing very flexible stellar anisotropy model for dSphs, and (3) running a large set of high-resolution simulations of the evolution of two-component dwarfs in the Galactic tidal field. We derive a sequence of cosmologically plausible models for Draco that are consistent with all the observed structural and kinematical properties of this dwarf. Our results are consistent with either of the two above solutions for the missing satellite problem.

2. GLOBAL CONSTRAINTS ON DRACO DM HALO PROPERTIES

We consider two types of DM halos: theoretically motivated Navarro-Frenk-White (1997, hereafter NFW) halos with a $\gamma = -1$ density cusp at the center, and observationally motivated Burkert (1995) halos, which have a flat core:

$$\rho(r) = \frac{\rho_s}{r/r_s (1 + r/r_s)^2} \quad (\text{NFW}), \quad (1)$$

$$\rho(r) = \frac{\rho_s}{(1 + r/r_s) [1 + (r/r_s)^2]} \quad (\text{Burkert}). \quad (2)$$

Here ρ_s and r_s are the scaling density and radius. At large distances from the center both halos have the same asymptotic density slope of $\gamma = -3$.

Analysis of cosmological N -body simulations showed that the concentration $c = r_{\text{vir}}/r_s$ of low-mass DM halos (with the virial mass $m_{\text{vir}} = 10^8 - 10^{11} M_\odot$) has a lognormal distribution with the mean

$$c = \frac{27}{1+z} \left(\frac{m_{\text{vir}}}{10^9 M_\odot} \right)^{-0.08} \quad (3)$$

and dispersion 0.14 dex (Bullock et al. 2001, with the correction of Sternberg et al. 2002). Here r_{vir} is the virial radius of the halo and z is the redshift.

Sternberg et al. (2002) showed that the four dwarf galaxies with a Burkert DM halo profile studied by Burkert (1995) have the same dependence of the DM halo scaling density ρ_s on the scaling radius r_s as do the NFW halos in cosmological simulations. This result was obtained for $z = 0$. We assume that it holds true for other redshifts as well, and use equation (3) to find concentrations of both NFW and Burkert halos.

Using the formula of Sheth & Tormen (1999), one can estimate the comoving number density of DM halos per unit $\ln m_{\text{vir}}$ and per standard deviation in concentration:

$$F \equiv \frac{dn}{d \ln m_{\text{vir}} d\nu_c} = \frac{0.322}{2\pi} \left(1 + \frac{1}{\nu^{0.6}} \right) \frac{\rho_m \nu}{S} \left| \frac{dS}{dm_{\text{vir}}} \right| \exp \left(-\frac{\nu^2 + \nu_c^2}{2} \right). \quad (4)$$

Here ν_c is the number of standard deviations from the mean concentration, $\nu = (0.707/S)^{1/2} \delta(z)$, where $\delta(z)$ is the critical over-

density for spherical collapse extrapolated linearly to $z = 0$, ρ_m is the present day mass density of the universe, and S is the variance of the primordial density field on mass scale m_{vir} extrapolated linearly to $z = 0$. To estimate the above parameters we follow Mashchenko et al. (2005). Throughout this paper we assume a flat Λ CDM cosmology and use the following values of the cosmological parameters: $\Omega_m = 0.27$, $\Omega_b = 0.044$, $H = 71 \text{ km s}^{-1} \text{ Mpc}^{-1}$, and $\sigma_8 = 0.84$ (Spergel et al. 2003).

It is interesting that one can derive quite general and (stellar) model-independent constraints on the properties of the Draco DM halo by combining the available observational data on this galaxy with the predictions of cosmology. Throughout this paper we assume that the distance to Draco is $82 \pm 6 \text{ kpc}$ (Mateo 1998). It is convenient to consider different DM halo constraints in the plane of two scaling parameters, ρ_s and r_s . We summarize the global constraints in Figure 1.

The most obvious constraint is that the Draco DM halo should have formed before the bulk of the Draco stars formed. We assume that the first star burst in Draco took place at least 10 Gyr ago (Mateo 1998), or at $z \geq 1.8$. In Figure 1 the areas to the right of the dashed lines marked “ $z = 1.8$ ” correspond to halos older than 10 Gyr.

The next constraint, $F \geq F_{\text{min}}$, comes from the requirement for DM halos to be abundant enough to explain the observed number (~ 20) of dwarf spheroidal galaxies in the Local Group. Following Mashchenko et al. (2005), we adopt $F_{\text{min}} = 0.01 \text{ Mpc}^{-3}$. As the function F does not explicitly depend on ρ_s and r_s (it depends on m_{vir} and z), in Mashchenko et al. (2005), we designed a numerical method for finding the most probable combination of (m_{vir}, z) corresponding to given values of (ρ_s, r_s) . As a by-product we also obtain the corresponding value of ν_c . The areas below the solid lines in Figure 1 correspond to DM halos that were abundant enough to have been progenitors of dwarf spheroidals in the Local Group.

Assuming that the tidal field of the Milky Way has not perturbed significantly the stars in the outskirts of Draco out to a distance of $r_{\text{out}} \sim 1.2 \text{ kpc}$ from its center (the last observed point in the Draco surface brightness profile of Odenkirchen et al. 2001; see Fig. 2a), the third constraint can be written as $r_{\text{vir}} \geq r_{\text{out}}$. (It is hard to imagine stars forming beyond the virial radius of its DM halo.) The halos in the areas above the dash-dotted lines in Figure 1 satisfy the above criterion.

In Figure 3 we plot the observed line-of-sight velocity dispersion profile for Draco (from Wilkinson et al. 2004). It has been noted that in Draco and Ursa Minor the galactic outskirts appear to be kinematically cold (Wilkinson et al. 2004). There appears to be no good explanation for this phenomena. Given the fact that in the case of Draco the only (outermost) radial bin that is “cold” contains only six stars with measured line-of-sight velocities, and is marginally (at $\sim 1 \sigma$ level) consistent with the global average for Draco, $\langle \sigma_{\text{los}} \rangle = 9.5 \text{ km s}^{-1}$, we decided to exclude the last bin from our analysis. Our assumption is that at the distance of $r_1 = 0.74 \text{ kpc}$ from the Draco center (halfway between the two last points in Fig. 3) the line-of-sight velocity dispersion for Draco is roughly equal to the global average:¹ $\sigma_{\text{los}}(r_1) \sim 9.5 \text{ km s}^{-1}$ (Fig. 3, *circle with a cross*). At this distance the stellar density in Draco is steeply declining (see Fig. 2a). As a result, most of stars observed at the projected distance r_1 from Draco’s center are located roughly in the plane of the sky at the *spatial* distance r_1 from the center of the dwarf. We can then use $\sigma_{\text{los}}(r_1)$ as a lower limit of Draco circular velocity at this

¹ This is consistent with the results of Munoz et al. (2005), who observed Draco to have $\sigma_{\text{los}} \sim 10 \text{ km s}^{-1}$ out to a distance of $\sim 1 \text{ kpc}$ from the center.

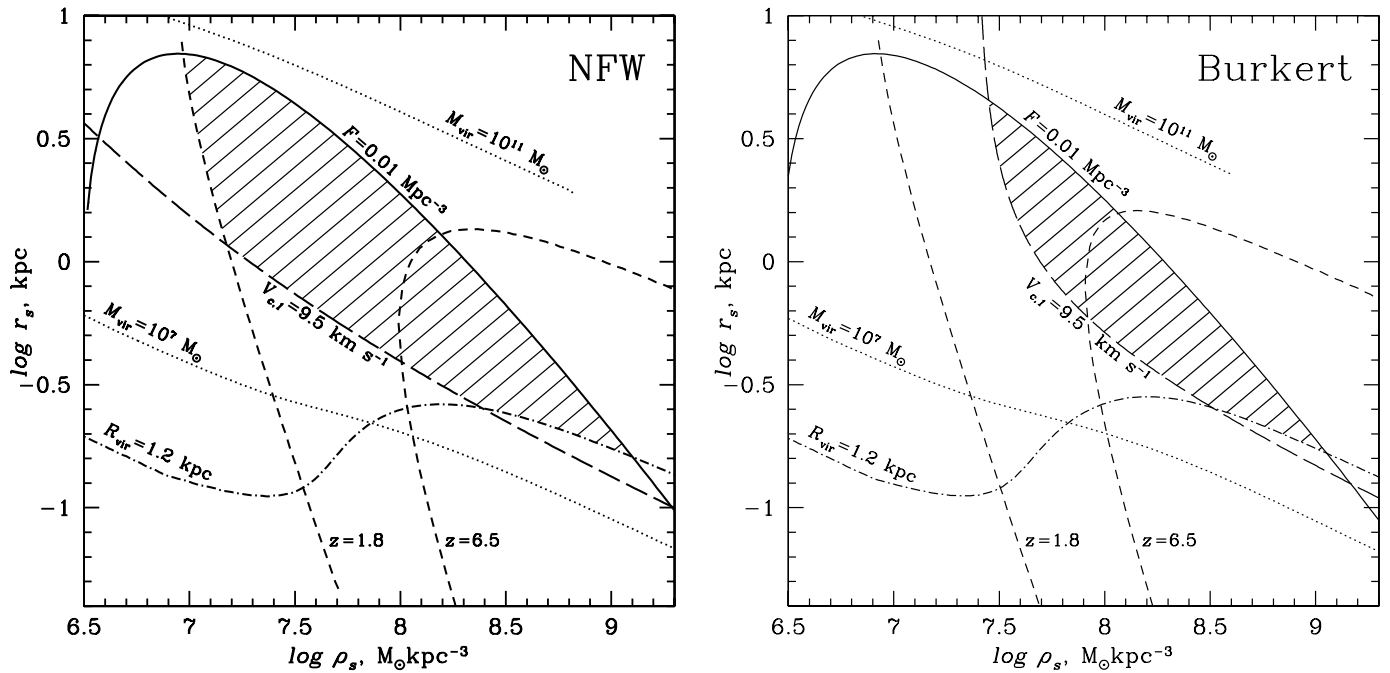


FIG. 1.—Exclusion plots for Draco DM halo parameters ρ_s and r_s . (Both NFW case [left panel] and Burkert case [right panel] are shown.) The hatched areas correspond to DM halos that satisfy all global constraints. Here $V_{c,1}$ is the circular speed at the distance $r_1 = 0.74$ kpc from the center of the halo.

distance, $V_{c,1}$. Indeed, if one considers the extreme of purely radial orbits, the line-of-sight velocity dispersion at large distance from the galactic center will be close to zero. In the opposite extreme of purely circular orbits, one can show that σ_{los} becomes approximately equal to the circular velocity at this distance. We plot the solution of the equation $V_{c,1} = 9.5 \text{ km s}^{-1}$ as long-dashed lines in Figure 1. The areas above these lines correspond to halos that satisfy the above criterion. The result we derived here is approximate, but of model-independent nature. We present more

accurate (but also more model-dependent) treatment in § 3, where we fit stellar models to all the reliable observed σ_{los} points in Figure 3.

The last constraint is that the virial mass of the Draco halo is somewhere between “ridiculously” low and high values 10^7 and $10^{11} M_\odot$ (Fig. 1, area between dotted lines). The lower limit is even lower, by a factor of 2–3, than the classical “mass follows light” estimates (Mateo 1998; Odenkirchen et al. 2001). The upper limit corresponds to a satellite that would very quickly spiral in

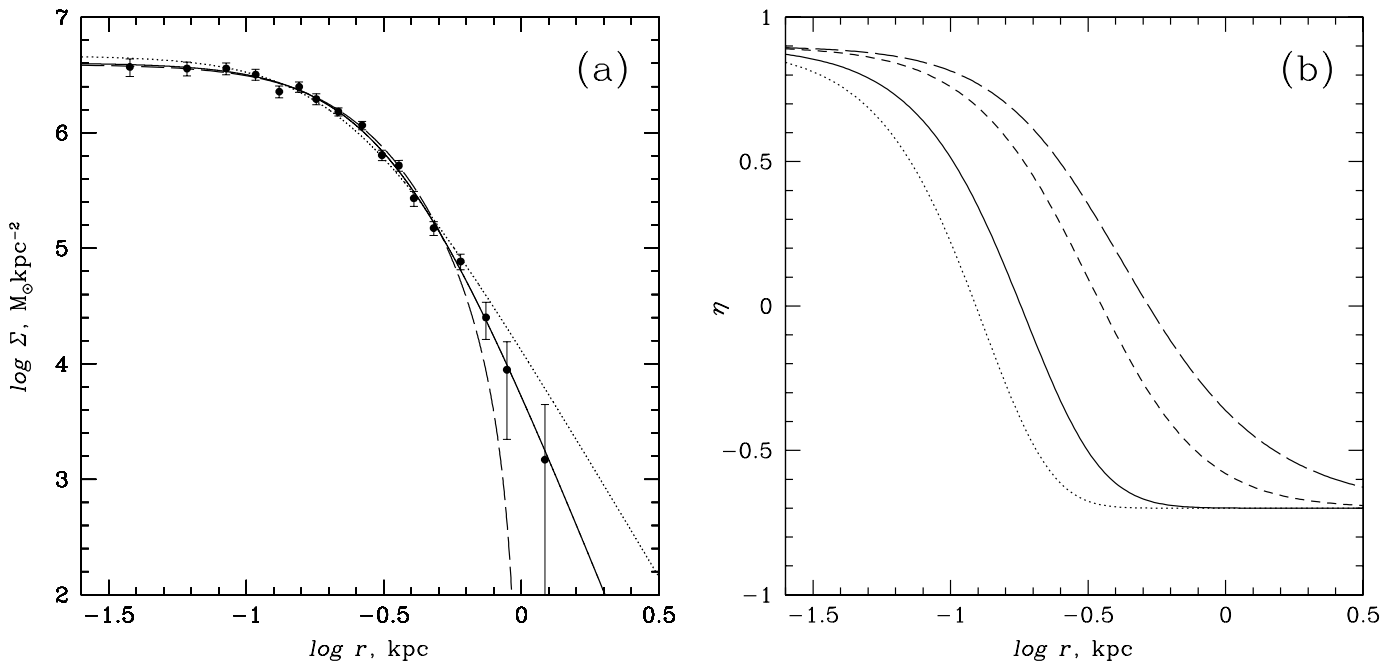


FIG. 2.—(a) Stellar surface density profiles for Draco. The observed profile of Odenkirchen et al. (2001), their sample S2 is shown as solid circles with 1σ error bars. The best-fitting profiles for a Plummer-like model with $\alpha = 7$, the Plummer model, and the King model are shown as solid, dotted, and dashed lines, respectively. (b) Stellar anisotropy profile $\eta(r)$ for the best-fitting Draco model with NFW DM halo ($\alpha = 7$, $\log \rho_s = 7.2$, $\log r_s = 0.45$, $\lambda = 1$, $\eta_0 = 0.9$, $\eta_1 = -0.7$) is shown as a solid line. For comparison, anisotropy profiles are shown for other values of λ : 0.5 (dotted line), 3 (short-dashed line), and 5 (long-dashed line).

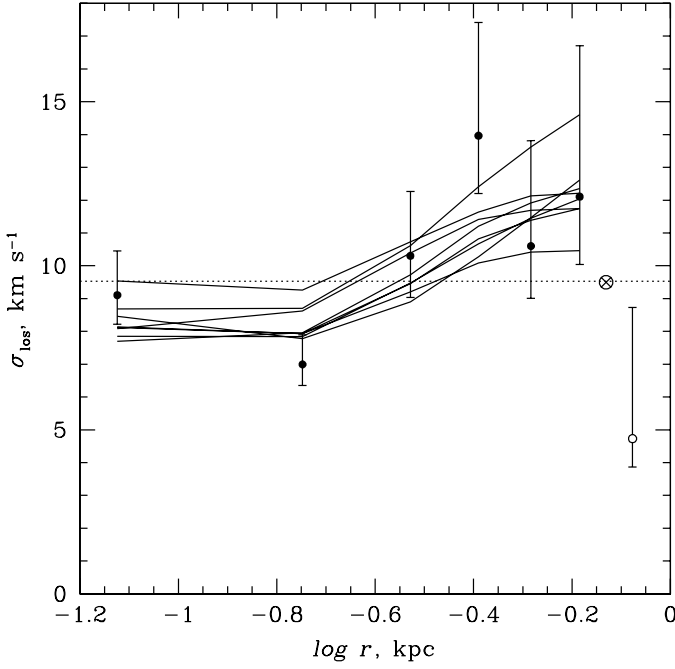


FIG. 3.—Line-of-sight stellar velocity dispersion profile for Draco. Observational data of Wilkinson et al. (2004) are shown as circles with 1σ error bars. The last point, which we consider to be unreliable, is shown as an open circle with error bars. The horizontal dotted line marks the global $\sigma_{\text{los}} = 9.5 \text{ km s}^{-1}$ for Draco. The σ_{los} profiles for our eight best-fitting stellar models are shown as solid lines. The big circle with a cross shows our assumption for σ_{los} at the distance of $r_1 = 0.74 \text{ kpc}$ from the Draco center.

to the center of the Milky Way due to dynamical friction. As one can see, the last constraint does not add any new information to our exclusion plots in Figure 1.

From comparison of Figures 1a and 1b one can see that all the constraints except for the fourth one ($V_{c,1} \geq 9.5 \text{ km s}^{-1}$) are very similar for both NFW and Burkert DM density profiles. This is intimately linked to our assumption that for a given virial mass m_{vir} and redshift z both types of halos have the same concentration—given by equation (3). This automatically makes the scaling radii r_s equal in both cases. At the same time, one can show that the scaling densities for NFW and Burkert halos are related through

$$\frac{\rho_{s,\text{Burkert}}}{\rho_{s,\text{NFW}}} = 2 \frac{\ln(1+c) - c/(1+c)}{\ln(1+c) + [\ln(1+c^2)]/2 - \arctan c}, \quad (5)$$

which is close to unity for realistic halos (the ratio changes from 0.966–0.921 for $c = 3.5$ –10). The fourth constraint, unlike the rest of the criteria, does not deal with a global property of a halo (such as m_{vir} and z or their derivatives, r_{vir} and F). Instead, it deals with the average DM density within a certain fixed radius—which can be dramatically different for cuspy NFW and flat-cored Burkert models.

The hatched areas in Figure 1 correspond to DM halos that satisfy all of the above global constraints. As one can see, the Draco halo parameters are not particularly well constrained, especially in the case of the NFW profile. Still, one can make a few interesting observations. First, the most restrictive (and useful) constraints are $F \geq 0.01 \text{ Mpc}^{-3}$ and $V_{c,1} \geq 9.5 \text{ km s}^{-1}$. Second, there is plenty of room for Draco to have formed before the end of the reionization of the universe at $z \sim 6.5$ (hatched areas to the right of the dashed lines marked “ $z = 6.5$ ” in Fig. 1). Third, we can derive the range of possible values of different halo

parameters. For NFW halos, our exclusion plot implies that $\log m_{\text{vir}} = 7.7$ –10.7, $z = 1.8$ –11, $r_s = 0.16$ –7.8 kpc, and $\log \rho_s = 7.0$ –9.1. (Here units for m_{vir} and ρ_s are M_\odot and $M_\odot \text{ kpc}^{-3}$, respectively.) For Burkert halos, $\log m_{\text{vir}} = 7.8$ –10.5, $z = 3.9$ –11, $r_s = 0.17$ –5.0 kpc, and $\log \rho_s = 7.4$ –9.1. Interestingly, for both NFW and Burkert cases, Draco could not have formed before $z \sim 11$, or more than 13.2 Gyr ago. The reason for that is that at larger redshifts DM halos with the virial radii $\geq 1.2 \text{ kpc}$ become too rare to correspond to a typical dwarf spheroidal galaxy in the Local Group.

The main purpose of generating the exclusion plots in Figure 1 was to significantly reduce the computational burden in the next step of our analysis, described in the next section, where we use the whole observed line-of-sight velocity dispersion profile along with the surface brightness profile to find the best-fitting stellar models and to further reduce the uncertainty in (ρ_s, r_s) values for the Draco DM halo.

3. STELLAR MODEL

The equilibrium state of a spherically symmetric stellar system can be described by the Jeans equation,

$$\frac{1}{\rho_*} \frac{d(\rho_* \sigma_r^2)}{dr} + \frac{2}{r} (\sigma_r^2 - \sigma_t^2) = -\frac{d\Phi}{dr} \quad (6)$$

(Binney & Tremaine 1987), which is obtained by taking the first velocity moment of the collisionless Boltzmann equation. Here r is the distance from the center of the system, ρ_* is the stellar density, σ_r and σ_t are the one-dimensional stellar radial and tangential velocity dispersions, respectively, and Φ is the total gravitational potential (due to stars and DM). The radial gradient of the gravitational potential can be calculated as $d\Phi/dr = G[m(r) + m_*(r)]/r^2$, where $m(r)$ and $m_*(r)$ are the enclosed DM and stellar masses, respectively, and G is the gravitational constant. From equations (1) and (2) we derived

$$m(r) = 4\pi r_s^3 \rho_s [\ln(1+x) - x/(1+x)] \quad (\text{NFW}), \quad (7)$$

$$m(r) = 2\pi r_s^3 \rho_s \times [\ln(1+x) + (1/2) \ln(1+x^2) - \arctan x] \quad (\text{Burkert}). \quad (8)$$

Here $x \equiv r/r_s$. We neglect impact of baryons on DM distribution, as in Draco the stellar density is more than an order of magnitude lower than DM density even at the center of the galaxy.

The Plummer density profile,

$$\rho_* = \rho_0 [1 + (r/b)^2]^{-5/2} \quad (9)$$

(Binney & Tremaine 1987), is used sometimes to describe simple spherically symmetric stellar systems, such as globular clusters and dwarf spheroidal galaxies. It has a core of size b and a power-law envelope with the slope $\gamma = -5$. We found that a “generalized Plummer law,”

$$\rho_* = \rho_0 [1 + (r/b)^2]^{-\alpha/2}, \quad (10)$$

which has a surface density profile of the form

$$\Sigma = \Sigma_0 [1 + (R/b)^2]^{-(\alpha-1)/2}, \quad (11)$$

provides much better fit to the Draco star count profile of Odenkirchen et al. (2001) than the Plummer model and the

theoretical King (1966) model, if one chooses $\alpha = 7$ (see Fig. 2a).² Here α is an integer number ≥ 2 and R is the projected distance from the center of the system. For $\alpha \geq 4$, the total stellar mass can be calculated as

$$M_* = \frac{2\pi\Sigma_0 b^2}{\alpha - 3}. \quad (12)$$

For $\alpha = 7$, the stellar enclosed mass is

$$m_*(r) = \frac{4\pi\rho_0 r^3}{15} \frac{5 + 2(r/b)^2}{(1 + r^2/b^2)^{5/2}}, \quad (13)$$

and $\rho_0 = 15\Sigma_0/(16b)$. The χ^2 fitting of equation (11) to the Draco profile of Odenkirchen et al. (2001) gave $\rho_0 = 1.08 \times 10^7 M_\odot \text{ kpc}^{-3}$ and $b = 0.349 \text{ kpc}$. (We assumed that the stellar V -band mass-to-light ratio of Draco stars is $\Upsilon = 1.32$, which is an average value of the Salpeter and composite model estimates of Mateo et al. 1998.)

Traditionally, in equation (6) one uses σ_r and $\beta \equiv 1 - \sigma_t^2/\sigma_r^2$ instead of σ_r and σ_t . The anisotropy parameter β is equal to $-\infty$, 0, and 1 for purely tangential (circular), isotropic, and purely radial stellar orbits. We advocate a different anisotropy parameter,

$$\eta \equiv \frac{\sigma_r^2 - \sigma_t^2}{\sigma_r^2 + \sigma_t^2}. \quad (14)$$

Unlike β , parameter η is symmetric: it is equal to -1 , 0, and 1 for circular, isotropic, and purely radial orbits. The equations connecting β and η are $\eta = \beta/(2 - \beta)$ and $\beta = 2\eta/(1 + \eta)$. Another useful expression is $\sigma_t^2 = \sigma_r^2(1 - \eta)/(1 + \eta)$. The Jeans equation (6) can now be rewritten as

$$\frac{1}{\rho_*} \frac{d(\rho_* \sigma_r^2)}{dr} + \frac{4\eta}{1 + \eta} \frac{\sigma_r^2}{r} = -\frac{d\Phi}{dr}. \quad (15)$$

As there are two unknown functions in equations (6) or (15), $\sigma_r(r)$ and $\sigma_t(r)$ (or $\beta[r]$, or $\eta[r]$), one customarily assumes the shape of the anisotropy profile and then solves the ordinary differential equation for $\sigma_r(r)$. The boundary condition is $\sigma_r(r \rightarrow \infty) = 0$. Traditional choices for the anisotropy profile are (1) $\beta = \text{constant}$ (with the special case of $\beta = 0$, or isotropic stellar orbits), and (2) the Osipkov-Merritt profile (Osipkov 1979; Merritt 1985),

$$\beta = \left[1 + (r_a/r)^2\right]^{-1}. \quad (16)$$

In the latter case, the stellar system is isotropic at the center, reaches $\beta = 0.5$ at $r = r_a$, and becomes purely radially anisotropic in infinity. Unfortunately, the two above choices are very limited. We propose instead a much more flexible anisotropy profile,

$$\eta = \eta_0 + (\eta_1 - \eta_0) \left[1 - (\rho_*/\rho_0)^{1/\lambda}\right], \quad (17)$$

which is applicable to systems with a flat core (such as a generalized Plummer model or King model). Here λ is a positive number of order of unity, and η_0 and η_1 are asymptotic values of the anisotropy parameter η for $r \rightarrow 0$ and $r \rightarrow \infty$, respectively. As one can see, the profile in equation (17) does not explicitly

depend on r , like the Osipkov-Merritt profile. Instead, it depends on the stellar density ρ_* . We believe it is a reasonable approach, as in many realistic stellar systems the same dynamical processes shape simultaneously both density and anisotropy profiles. The examples are the collapse of initially homogeneous warm stellar sphere (van Albada 1982; Mashchenko & Sills 2005a) and the expansion of a newly formed stellar system in a spherical galaxy with a DM halo after removal of the leftover gas by the feedback mechanisms (Mashchenko et al. 2005). In both cases, the stellar orbits become increasingly radially anisotropic in the outskirts of the relaxed system, where the density is steeply declining.

Both $\beta = \text{constant}$ and the Osipkov-Merritt profiles can be considered as special cases of our more general expression in equation (17). Indeed, fixing $\eta_0 = \eta_1$ would correspond to the case of $\beta = \text{constant}$; using the generalized Plummer density profile from equation (10) and setting $\lambda = \alpha/2$ produces the Osipkov-Merritt profile with $r_a = b/\sqrt{2}$.

The parameter λ in equation (17) controls how sensitive the anisotropy parameter is to changes in density. To illustrate this effect, in Figure 2b we show anisotropy profiles for Draco with $\eta_0 = 0.9$, $\eta_1 = -0.7$, and $\lambda = 0.5, 1, 3, 5$. One can see that by varying λ by a factor of a few a large range of possible anisotropy profiles is produced.

We designed a numerical algorithm to find values of the parameters controlling the shape of the anisotropy function η (η_0 , η_1 , and λ) that would χ^2 -minimize the deviation of the simulated line-of-sight velocity dispersion profile from the observed one (Fig. 3, *circles with error bars*; we excluded from our analysis the last point as an unreliable one) for given ρ_s , r_s , and the halo profile (NFW or Burkert). The procedure consists of the following six steps:

1. We choose values of $\log \rho_s$ and $\log r_s$ from a grid with spacings of 0.45 and 0.15 dex, respectively. (The values of the increments were chosen to lead to a factor of 2 increase in the halo virial mass.) The reference point of the grid is $\log \rho_s = 9$ and $\log r_s = 0$. Only those grid points that lie within the hatched zones in Figure 1 are considered. In the Burkert case, we also considered a few points lying outside of the hatched area in attempt to bracket the point with the best χ^2 . All these grid points are shown as circles (either open or filled) in Figure 4. Overall, we considered 35 different DM halo models.

2. For each of the DM halo models, we consider 1764 different combinations of anisotropy shape parameters $\eta_0 = -1, -0.9, -0.8, \dots, 1$, $\eta_1 = -1, -0.9, -0.8, \dots, 1$, and $\lambda = 0.5, 1, 3, 5$. For each combination, we solve the Jeans equation (15) numerically with the anisotropy, stellar density, enclosed DM mass, and enclosed stellar mass profiles given by equations (17), (9), (7) and (8), and (13), respectively. We adopt $\alpha = 7$, $\rho_0 = 1.08 \times 10^7 M_\odot \text{ kpc}^{-3}$, and $b = 0.349 \text{ kpc}$. The solution of the Jeans equation is the radial velocity dispersion profile $\sigma_r(r)$.

3. For each of the above $\sim 60,000$ models we generate a spherically symmetric N -body stellar model, with the number of particles $N = 10,000$. Stellar particles are distributed randomly, with the density profile given by equation (9). Each stellar particle is assigned random values of the radial and two tangential components of the velocity vector: V_r , V_θ , and V_ϕ . All three components are assumed to have a Gaussian distribution, with the dispersions $\sigma_r(r)$, $\sigma_t(r)$, and $\sigma_t(r)$, respectively. This is an approximate method of generating a close-to-equilibrium N -body system with an arbitrary density and anisotropy profiles. The accurate method would involve numerically calculating the distribution function, which is a very computationally expensive procedure. This would render our approach unfeasible.

² For the Draco star count of Wilkinson et al. (2004) the best-fitting value of α is 6.

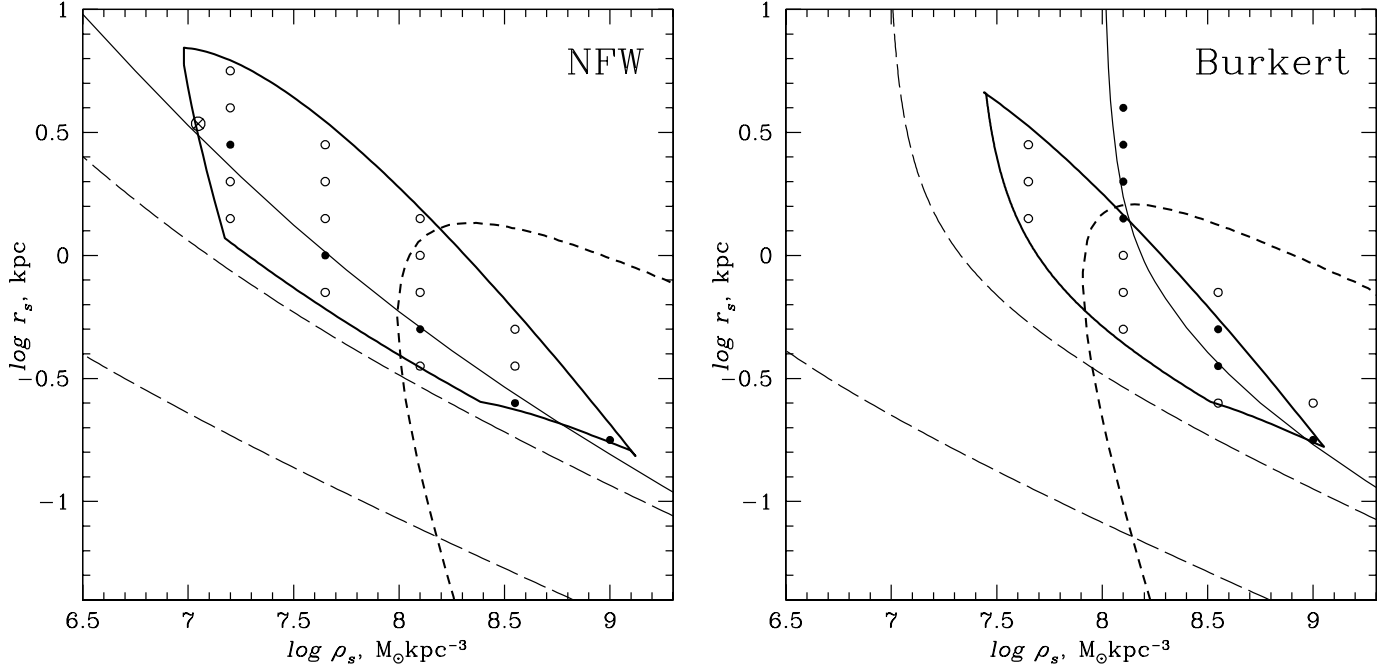


FIG. 4.—Best-fitting stellar models for different Draco DM halo parameters ρ_s and r_s . Filled (open) circles correspond to models that have $\chi^2 < 9.5$ ($\chi^2 > 9.5$) between the modeled and observed line-of-sight velocity dispersion profiles. Thick solid lines mark the areas where all the global constraints on (ρ_s, r_s) are satisfied (see Fig. 1). Thin solid lines correspond to isothermal stellar models with $\sigma = 9.5 \text{ km s}^{-1}$. Short-dashed lines correspond to halos formed at $z = 6.5$. Long-dashed lines correspond to halos with the analytical tidal radius equal to 0.85 kpc for the extreme values of the orbital pericentric distance, $R_p = 2.5$ and 70 kpc (see § 4.1). The circle with a cross marks the best-fitting Draco model from Mashchenko et al. (2005) for the Draco surface brightness profile of Odenkirchen et al. (2001).

4. We calculate the line-of-sight velocity dispersion profile for the generated N -body stellar models integrated over the same projected radial bins as in the observed profile of Wilkinson et al. (2004) (the edges of their bins are 0, 0.12, 0.24, 0.36, 0.48, 0.60, 0.72 kpc; J. Kleyna 2005, private communication). For this we use the projection method of Mashchenko & Sills (2005a, their Appendix B), where we explicitly use the spherical symmetry of our stellar system.

5. We calculate χ^2 difference between the observed line-of-sight velocity dispersion profile (the six reliable points in Fig. 3) and the modeled one. As the observational error bars are asymmetric, for calculating χ^2 we use the appropriate one-sided value of the standard deviation depending on which side of the observed point the model point is located.

6. For each DM halo model, we choose one of 1764 models, with different η_0, η_1 , and λ , which produces the lowest value of χ^2 .

For most DM halo models, we could not find a good fit to the observed line-of-sight velocity dispersion profile (with some models having $\chi^2 > 100$): all modeled $\sigma_{\text{los}}(r)$ points were either well above or well below the observed ones. Only a few models produced $\chi^2 < 9.5$ (Fig. 4, *filled circles*). It is interesting that for both NFW and Burkert cases the best-fitting models follow very closely a sequence of isothermal stellar models with the total one-dimensional stellar velocity dispersion $\sigma_{\text{tot}} = [(\sigma_r^2 + 2\sigma_t^2)/3]^{1/2} = 9.5 \text{ km s}^{-1}$ (Fig. 4, *thin solid lines*). We obtained the isothermal solutions by solving the appropriate Jeans equation,

$$\frac{1}{\rho_*} \frac{d(\rho_* \sigma_r^2)}{dr} + \frac{3}{r} (\sigma_r^2 - \sigma_{\text{tot}}^2) = -\frac{d\Phi}{dr}, \quad (18)$$

with the boundary condition $\sigma_r(0) = \sigma_{\text{tot}}$. For isothermal systems the usual Jeans equation requirement $\sigma_r(r \rightarrow \infty) = 0$ does not hold in general case, and at some radius r_{max} the solution breaks down when σ_r^2 becomes negative. The isothermal model lines

shown in Figure 4 were obtained by finding the value of r_s that would maximize r_{max} for given ρ_s . Typically $r_{\text{max}} \gg 1 \text{ kpc}$, and only for the NFW model with $\rho_s = 10^9 M_\odot \text{ kpc}^{-3}$ did it drop down to 0.6 kpc.

The closeness of our best-fitting models to isothermal models does not imply that the isothermal models are the best ones. We calculated χ^2 differences between the observed and modeled line-of-sight velocity dispersion profiles for a few isothermal models, and they were substantially worse than for our best-fitting models. We also plotted $\sigma_{\text{tot}}(r)$ profiles for the best-fitting models, and they were not isothermal. The explanation for the closeness of our best-fitting models to the isothermal ones is in the virial theorem. Given that the line-of-sight velocity dispersion profile and the surface brightness profile are fixed, the virial theorem implies that all realistic models should stay close to a certain line in the (ρ_s, r_s) plane.

From Figure 4 one can see that the best-fitting models are well bracketed inside the zones where all the global constraints on ρ_s and r_s from § 2 are satisfied. In other words, we have a good agreement between the global constraints and the detailed $\sigma_{\text{los}}(r)$ analysis constraints, which were derived in a very different fashion. The exception is the Burkert halos with $\log \rho_s = 8.1$, where χ^2 is slightly improving when moving upward into the area with $F < 0.01 \text{ Mpc}^{-3}$. This is explained by the fact that at this value of $\log \rho_s$ the isothermal sequence is making a sharp upward turn.

We list the parameters for the best-fitting models in Table 1. We show only the models with $\chi^2 < 9.5$ located within the globally constrained zones. As for the Burkert halos with $\log \rho_s = 8.55$, we have two comparably good models, and we chose the one that is closer to the isothermal sequence.

Analysis of Table 1 shows that a comparably good $\sigma_{\text{los}}(r)$ fit can be obtained for a very large range in virial masses, from $\sim 7 \times 10^7$ to $\sim 5 \times 10^9 M_\odot$, for both NFW and Burkert halos. Despite very large difference in DM masses and density profiles, all the best-fitting stellar models have comparable values

TABLE 1
BEST-FITTING STELLAR MODELS

MODEL	INPUT PARAMETERS					DERIVED PARAMETERS									
	Halo	$\log \rho_s$ ($M_\odot \text{ kpc}^{-3}$)	$\log r_s$ (kpc)	N_{DM}	ϵ_{DM} (pc)	λ	η_0	η_1	χ^2	m_{vir} (M_\odot)	z	c	r_{vir} (kpc)	ν_c	$\log F$ (Mpc^{-3})
N1.....	NFW	7.20	0.45	10^6	60	1	0.9	-0.7	5.4	4.6×10^9	2.46	5.55	15.6	-0.68	-1.09
N2.....	NFW	7.65	0.00	3.16×10^5	28	1	0.7	-0.8	6.6	5.2×10^8	4.50	4.80	4.80	-0.23	-0.15
N3.....	NFW	8.10	-0.30	10^5	36	1	0.8	-0.9	6.1	1.8×10^8	7.10	4.55	2.28	0.54	0.08
N4.....	NFW	8.55	-0.60	10^5	20	1	0.6	-1.0	8.9	6.9×10^7	9.45	5.14	1.29	1.47	-0.11
N5.....	NFW	9.00	-0.75	10^5	19	1	1.0	-1.0	8.6	8.4×10^7	10.7	6.92	1.23	2.80	-1.62
B1.....	Burkert	8.10	0.15	10^6	37	1	0.7	0.0	6.6	4.5×10^9	6.74	4.98	7.03	1.48	-1.93
B2.....	Burkert	8.55	-0.45	3.16×10^5	30	1	0.7	-0.6	6.5	2.1×10^8	9.64	5.17	1.84	1.82	-0.97
B3.....	Burkert	9.00	-0.75	10^5	19	1	0.8	-0.9	6.2	9.1×10^7	11.0	6.91	1.23	2.90	-1.83

NOTE.—Here N_{DM} and ϵ_{DM} are the number of the DM particles and the gravitational softening length for DM particles in N -body simulations (see § 4.2).

of the anisotropy parameters: $\lambda = 1$ (in other words, anisotropy η is a linear function of the stellar density), $\eta_0 \sim 0.8$, and $\eta_1 \sim 0$ to -1 .

In Figure 3 we show the line-of-sight velocity dispersion profiles for the eight best-fitting models from Table 1 integrated over the same projected radial bins as the observed profile. All the models correctly reproduce the observational trend of a slight increase in σ_{los} with radius. However, two models with the largest virial mass (both NFW and Burkert) produce profiles that are rising rather steeply at the last measured point. This could present a problem if the result of Munoz et al. (2005), that the σ_{los} profile in the outskirts of Draco is almost flat, is confirmed with a larger sample of stars. For less massive models, the line-of-sight velocity dispersion profiles are leveling off at the last measured point, which is more in line with the results of Munoz et al. (2005).

Assuming that the best-fitting stellar models follow closely the isothermal sequence, from Figure 4 we can derive new (slightly better than in the previous section) constraints on Draco's DM halo parameters: $\log m_{\text{vir}} \simeq 7.9\text{--}9.7$ (for both NFW and Burkert halos), $z = 1.8\text{--}10$, $r_s = 0.21\text{--}3.1$ kpc, $\log \rho_s = 7.0\text{--}8.8$ (for NFW halos), and $z = 6.8\text{--}11$, $r_s = 0.18\text{--}1.4$ kpc, $\log \rho_s = 8.1\text{--}9.0$ (for Burkert halos). The interesting result is that if *cosmological halos have a Burkert-like flat-cored DM density profiles, then Draco should have formed before the end of the reionization of the universe at $z \sim 6.5$.*

4. EVOLUTION IN THE MILKY WAY POTENTIAL

4.1. Possible Orbits in the Galactic Potential

To carry out tidal stripping simulations for Galactic satellites, it is of principal importance to know reasonably well the shape of the gravitational potential of the Milky Way. One popular Milky Way model often used to calculate orbits of Galactic globular clusters and dwarf spheroidals is that of Johnston et al. (1999). This model consists of three components: (1) a disk represented by Miyamoto & Nagai (1975) potential with the mass $1.0 \times 10^{11} M_\odot$, radial scale-length 6.5 kpc, and scale-height 0.26 kpc; (2) a spherical bulge with a Hernquist (1990) potential, mass $3.4 \times 10^{10} M_\odot$, and scale-length 0.7 kpc; and (3) an isothermal halo with $\sigma = 128 \text{ km s}^{-1}$ and a flat core of size 12.0 kpc. The model was designed to reproduce the observed flat Galactic rotation curve between 1 and 30 kpc.

There are two major disadvantages of the above model for our work. First, it is axisymmetric, which adds an additional degree of freedom to our already multidimensional problem. (Orbits in axisymmetric potentials depend on all three components of the space

velocity vector of the satellite, whereas in spherical potentials orbits depend only on the radial, V_r , and tangential, V_t , space velocity components.) Second, the DM halo of Johnston et al. (1999) is an isothermal sphere with the rotation curve asymptotically approaching $V_c = 181 \text{ km s}^{-1}$ as $r \rightarrow \infty$, whereas in the cosmological halos the rotation curves are declining in the outskirts.

We decided to use a simple static NFW potential,

$$\Phi = -4\pi G \rho_s R_s^3 \ln(1 + R/R_s)/R, \quad (19)$$

as the Milky Way model for our project. The scaling radius R_s and density ρ_s of an NFW halo can be determined from the virial mass M_{vir} and concentration C . These quantities are still not very well known for the Milky Way. Traditionally, one uses different Galactic objects (stars, gas, globular clusters, dwarf spheroidals) with known line-of-sight velocity and, in some cases, proper motion as kinematical tracers of the Galactic potential, with different authors obtaining quite different results. The favored model of Klypin et al. (2002), for example, has a virial mass of $10^{12} M_\odot$ and concentration 10–17. Other recent NFW halo based models have $M_{\text{vir}} = (0.7\text{--}1.7) \times 10^{12} M_\odot$, $C = 5\text{--}12$ (Cardone & Sereno 2005), and $M_{\text{vir}} = (0.6\text{--}2.0) \times 10^{12} M_\odot$, $C = 18$ (Battaglia et al. 2005). The non-NFW models of Sakamoto et al. (2003) give larger values for the total mass of the Milky Way: $M_{\text{vir}} = (1.5\text{--}3.0) \times 10^{12} M_\odot$ if Leo I is gravitationally bound to the Galaxy, and $M_{\text{vir}} = (1.1\text{--}2.2) \times 10^{12} M_\odot$ if not.

We adopted an intermediate value for the Galactic virial mass, $M_{\text{vir}} = 1.5 \times 10^{12} M_\odot$. The median concentration of cosmological halos with such mass at $z = 0$ is $C = 13.2$ (Bullock et al. 2001). The halo scaling parameters are then $R_s = 22.6$ kpc and $\rho_s = 6.0 \times 10^6 M_\odot \text{ kpc}^{-3}$, and the virial radius is $R_{\text{vir}} = 298$ kpc.

The radial tidal acceleration $-d^2\Phi/dr^2$ of our NFW halo is comparable to that of the composite model of Johnston et al. (1999). As one can see in Figure 5, the tidal acceleration profile for the NFW halo is located between the two extreme profiles for the Johnston et al. (1999) model (in the Galactic plane and along the polar axis) down to a radius of ~ 10 kpc.

We obtained the pericentric and apocentric distances, R_p and R_a , for closed Draco's orbits in the potential given by equation (19) by solving numerically the following nonlinear equation (Binney & Tremaine 1987):

$$\frac{1}{R^2} + \frac{2[\Phi(R) - \Phi(R_0)] - V_r^2 - V_t^2}{R_0^2 V_t^2} = 0, \quad (20)$$

where R_0 , V_r , and V_t are the Draco's current distance from the Galactic center, radial velocity, and tangential velocity, respectively.

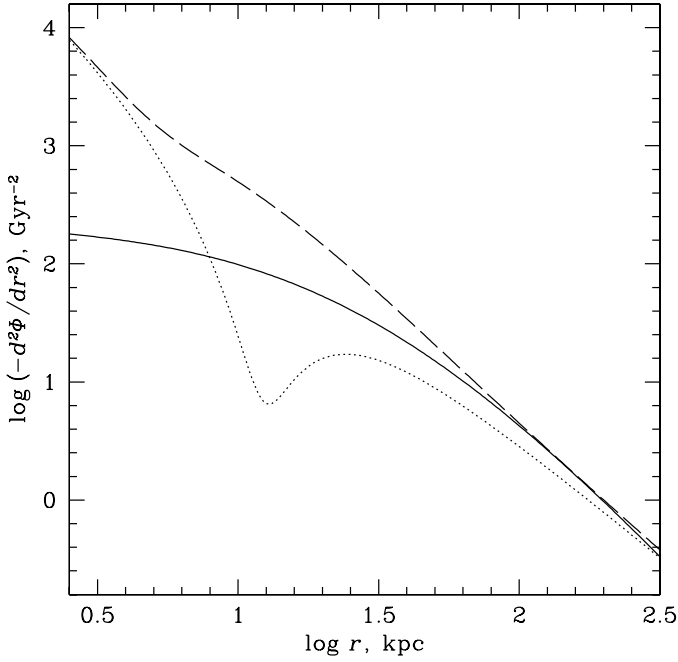
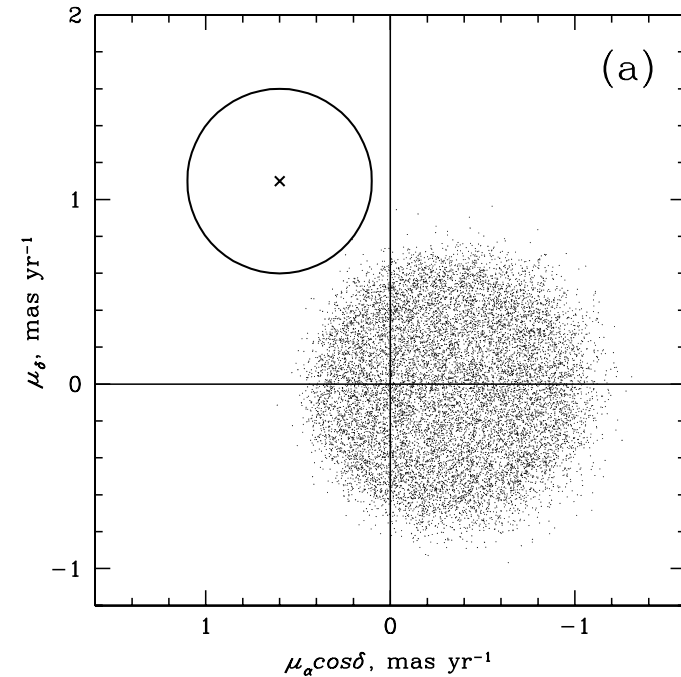


FIG. 5.—Radial tidal acceleration profiles for the Milky Way models. The solid line corresponds to our NFW model. The composite model of Johnston et al. (1999) is shown as dashed (in the Galactic plane) and dotted (in the polar direction) lines.

If proper motion is known, the two space velocity vector components V_r and V_t can be calculated using the procedure outlined in the Appendix. The radial orbital period is obtained by solving numerically the following integral (Binney & Tremaine 1987):

$$P = 2 \int_{R_p}^{R_a} \frac{dR}{\sqrt{V_r^2 + V_t^2 - 2[\Phi(R) - \Phi(R_0)] - R_0^2 V_t^2 / R^2}}. \quad (21)$$



Scholz & Irwin (1994) published the only available measurement of the proper motion of Draco: $\mu_\alpha \cos \delta = 0.6 \pm 0.5$ mas yr⁻¹, and $\mu_\delta = 1.1 \pm 0.5$ mas yr⁻¹. (We adopted the larger value for the uncertainty from the text of their paper.) When we started this project, we hoped that the measurements of Scholz & Irwin (1994) could be used to place useful constraints on possible Draco's orbits in the Milky Way potential. Unfortunately, this is not the case. This can be seen from Figure 6a, which shows the proper motion measurements of Scholz & Irwin (1994) and the locus of the possible proper motion vectors resulting in a closed orbit in the Milky Way potential given by equation (19). (We assumed that the halo density drops to zero beyond the virial radius r_{vir} , and took into account the uncertainties in the distance to Draco, $d = 82 \pm 6$ kpc, and its line-of-sight velocity, $V_{\text{los}} = -293 \pm 2$ km s⁻¹, which were taken from Mateo 1998.) One can see that the observational results are virtually inconsistent with Draco moving along a bound orbit around the Milky Way. More quantitatively, the chance for a bound orbit with the radial period $P < 8$ Gyr is only 5.5% (or 7.4% for any period, which includes periods much longer than the Hubble time). This is not surprising, as the proper motion measurements of Scholz & Irwin (1994) imply that Draco moves in the Galactic halo with a staggering speed of 610 ± 190 km s⁻¹ (1σ error bars), with no realistic Milky Way model being able to keep it gravitationally bound.

Given that Draco appears to be a pretty normal dwarf spheroidal galaxy and that the dwarf spheroidals strongly concentrate toward the two large spirals in the Local Group (Mashchenko et al. 2004), the Milky Way and the M31 galaxy, it seems to be very unlikely that this dwarf moves along an unbound orbit around our Galaxy, and just by chance happened to be at the present small distance from the Galactic center. We assume instead that Draco moves on a bound orbit, with $P \lesssim 8$ Gyr, and that the proper motion measurements of Scholz & Irwin (1994)

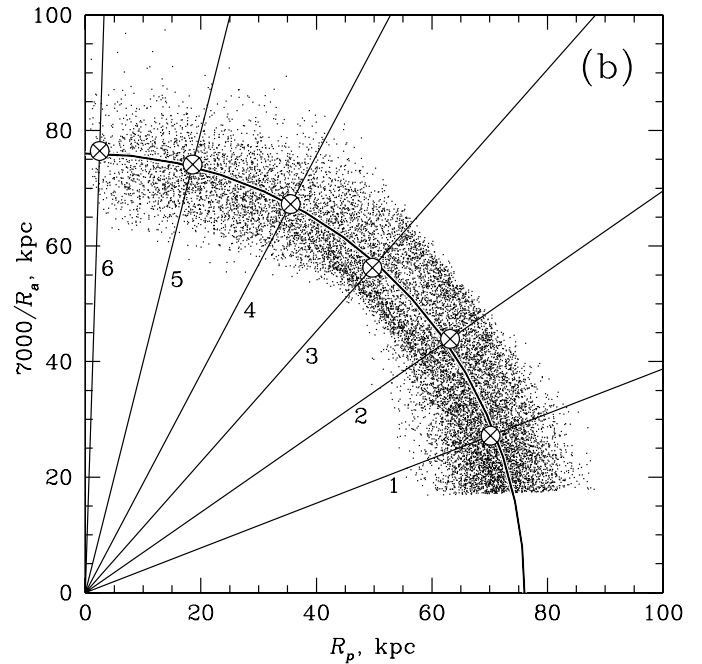


FIG. 6.—(a) Proper motion vectors for Draco. The observational result of Scholz & Irwin (1994) is shown as a cross with the circle representing a 0.5 mas yr^{-1} 1σ error bar. Dots correspond to proper motion vectors that result in a bound orbit with the period $P < 8$ Gyr in the Milky Way potential. (b) Draco's bound orbits with $P < 8$ Gyr in the $(R_p, 7000/R_a)$ coordinates (dots). In these coordinates, the orbits follow well a circle with a radius 76 kpc (thick solid line). The cutoff at $7000/R_a \sim 20$ kpc is due to the imposed cutoff in the orbital period $P < 8$ Gyr. For six different values of the polar angle θ (numbered radially divergent straight lines) we plot the averaged distances of the points from the reference point (circles with crosses). As one can see, all the averaged distances are very close to 76 kpc.

TABLE 2
DRACO'S ORBITS

Orbit	θ (rad)	R_p (kpc)	R_a (kpc)	R_a/R_p	P (Gyr)	$V_{l,a}$ (km s ⁻¹)	f_p
1.....	0.37	70.1	260	3.7	4.86	78.3	0.25
2.....	0.61	62.4	162	2.6	2.99	103.9	0.47
3.....	0.85	51.1	122	2.4	2.19	112.1	0.76
4.....	1.09	35.7	104	2.9	1.71	99.9	0.64
5.....	1.33	18.5	96.9	5.2	1.42	65.5	0.57
6.....	1.54	2.47	92.1	37	1.23	11.5	0.54

NOTE.—Here $V_{l,a}$ is the tangential velocity at $R = R_a$ and f_p is the fraction of the time Draco spends at the distances $R = 70\text{--}140$ kpc from the Galactic center, where 75% of Galactic dwarf spheroidals are currently located.

are wrong. Proper motion measurements of the outer Galactic halo objects based on heterogeneous collection of photographic plates spanning a few decades, such as those of Scholz & Irwin (1994), are notoriously difficult to correct for all possible sources of systematic errors. As another example, the proper motion measurement of the same authors (Scholz & Irwin 1994) for Ursa Minor is more than 1σ away from each of the three more recent results, including two derived with the help of the *Hubble Space Telescope* (Piatek et al. 2005, their Fig. 16).

Fortunately, even in the case when the proper motion is not known, some constraints can be placed on the orbital elements of Draco. We noticed that pericentric and apocentric distances for all the bound orbits from Figure 6a are not completely independent, and follow closely the solution of the equation

$$\left[R_p^2 + (7000/R_a)^2\right]^{1/2} = 76 \text{ kpc}, \quad (22)$$

which is a circle with a radius of 76 kpc in the coordinates $x = R_p$, $y = 7000/R_a$ (see Fig. 6b). (Here R_p and R_a are in kpc.) As one can see in Figure 6b, despite the observational un-

certainties in d and V_{los} and the fact that the proper motion is not known, Draco's bound orbits stay in a relatively narrow zone near the solution of equation (22). Neglecting the spread of the points around the circle, one can assume then that Draco's bound orbits form a one-dimensional family of models, with both R_p and R_a depending only on the polar angle θ , with $\tan \theta = y/x = 7000/(R_p R_a)$.

We chose six different values of the polar angle θ (shown as radially divergent lines in Fig. 6b, and listed in Table 2) to obtain a sequence of Draco's bound orbits. We used plots shown in Figure 7 to estimate the typical values of R_p and R_a corresponding to the particular values of the angle θ . In Table 2 we list the parameters of the derived Draco's orbits. The range of covered orbital periods is $\sim 1\text{--}5$ Gyr. All the orbits except for the last one have a pericenter at the distances where the tidal disruption properties of our NFW halo are comparable to those of the composite Milky Way model of Johnston et al. (1999) (see Fig. 5). Orbit 6 was designed to explore the extreme case of a virtually radial orbit. The apocenter of the orbit with the longest period is at 260 kpc, which is at the very edge of the virialized Galactic halo. As one can see from Table 2, the derived sequence of orbits is not trivial, with the orbits being more eccentric for the longest and shortest periods, and becoming rounder for intermediate periods of ~ 2 Gyr.

It is interesting to note that six out of eight, or 75%, of the "classical" Galactic dwarf spheroidals (we exclude Sagittarius as being currently tidally disrupted) are located in a rather narrow interval of Galactocentric distances $R = 70\text{--}140$ kpc (Mateo 1998). This includes Draco and excludes Leo I and II. In Table 2 we list for each orbit the fraction of time f_p Draco spends in this interval of Galactocentric distances. Statistically speaking, if Draco is a "normal" dwarf spheroidal, f_p should be around 0.75. Our orbit 3 is in this sense the likeliest orbit for Draco, and orbit 1 (and probably 2) is rather unlikely.

In Figure 4 we show as long-dashed lines the halos with the analytical tidal radius r_{tid} equal to 0.85 kpc, which is the radius where the density of Draco stars on the map of Odenkirchen

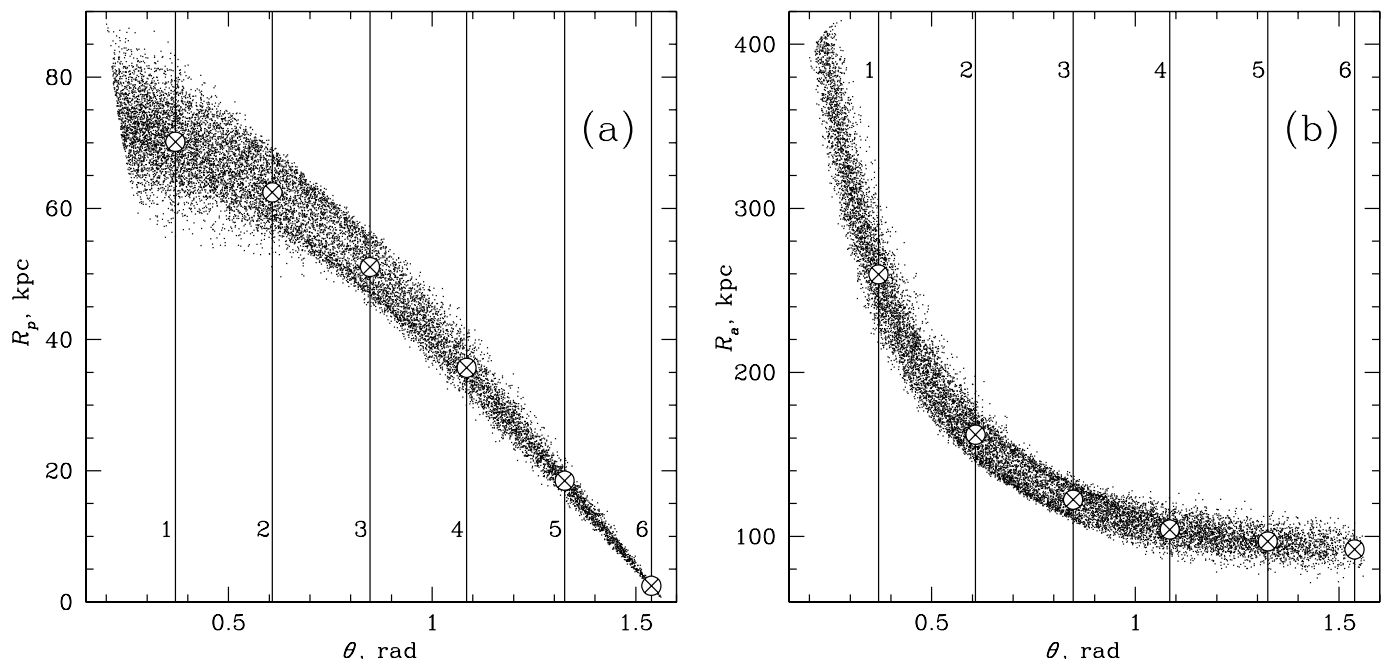


FIG. 7.—Our choices for Draco's orbits. Dots show bound orbits with $P < 8$ Gyr. Vertical lines correspond to the six different values of the polar angle θ from Fig. 6b. Circles with crosses mark the averaged orbital parameter (either pericentric distance R_p [panel a] or apocentric distance R_a [panel b]) values for different angles θ .

et al. (2001) is 2σ above the noise level. We calculated r_{tid} from

$$\frac{m(r_{\text{tid}})}{r_{\text{tid}}^3} = \left[2 - \frac{R}{M(R)} \frac{\partial M}{\partial R} \right] \frac{M(R)}{R^3} \quad (23)$$

(Hayashi et al. 2003), where $M(R)$ and $m(r)$ are the enclosed mass for the Milky Way and the satellite, respectively. Even at this large distance from Draco's center, Odenkirchen et al. (2001) did not see any sign of Draco being tidally distorted by the Milky Way tidal field. From Figure 4 one can see that all our best-fitting models (*solid circles*) have tidal radii larger than 0.85 kpc (even for the worst orbit with $R_p = 2.5$ kpc). One would naively conclude that the tidal forces are not important for our Draco models. But the reality is more complicated than that. Numerical N -body simulations of the evolution of subhalos orbiting in the host halo showed that removal of DM from the outskirts of the satellite results in the expansion of the satellite, which reduces its average density and exposes more DM to the action of the tidal field (Hayashi et al. 2003; Kazantzidis et al. 2004). Burkert halos have lower average density than NFW halos, and as a result are even easier to disrupt tidally (Mashchenko & Sills 2005b). Moreover, even well inside the tidal radius, distribution of bound stars can be noticeably distorted by the tidal field of the Milky Way, which would be at odds with the Draco observations of Odenkirchen et al. (2001). To correctly describe the above effects, we had to resort to high-resolution N -body simulations of the tidal disruption of our best-fitting composite (DM + stars) models from Table 1 in the static potential of the Milky Way. This is described in the following sections.

4.2. Isolated Models

To run the N -body simulations of the tidal stripping of Draco in the static gravitational potential of the Milky Way, we used the parallel tree-code Gadget-1.1 (Springel et al. 2001). We generated equilibrium DM halos for our eight models (see Table 1) using the prescription in Mashchenko & Sills (2005a). The essence of this approach is to use explicitly the distribution function (DF) to set up the initial distribution of velocity vectors of DM particles (isotropy was assumed). It was argued (Kazantzidis et al. 2004) that using DFs explicitly is far superior to traditional local Maxwellian approximation for cuspy models such as NFW. To reduce the boundary effects, we truncate DM halos at a distance of two virial radii r_{vir} from the center. This results in virtually no evolution for isolated models within the virial extent of the halos after 10 Gyr. We chose the gravitational softening lengths (separately for DM and stars) to be commensurable with the average interparticle distance: $\varepsilon = 0.77 r_h N^{-1/3}$ (Hayashi et al. 2003). Here r_h is the half-mass radius of the system. For stellar particles, $\varepsilon_* = 8.6$ pc. For DM particles, ε_{DM} values are listed in Table 1.

To set up the initial distribution of stars inside the DM halo, we use the same pseudo-Maxwellian approximation we used to measure the projected line-of-sight velocity dispersion profiles in § 3 (step 3). The only difference is that now we use a larger number of stellar particles, $N_* = 30,000$, to reduce the Poisson noise in the observable properties of the models.

Our baseline number of DM particles is $N_{\text{DM}} = 10^5$. Test runs showed that in the most massive models (N1 and N2, and B1 and B2) a much larger number of DM particles is required to prevent the artificial evolution of the stellar cluster at the center of the halo. We observed the central stellar density being significantly reduced (by more than an order of magnitude in the worst cases) in the low-resolution models. This effect does not

depend on the number of stellar particles and becomes less severe for larger N_{DM} and/or ε_{DM} . As stars are only a trace population in our models, the most obvious explanation for the above artifact is that stars get scattered from the imperfections of the granulated gravitational potential of the DM halo. Setting $N_{\text{DM}} = 10^6$ for models N1 and B1, and $N_{\text{DM}} = 3.16 \times 10^5$ for models N2 and B2 resulted in acceptable level of the artificial evolution of the surface brightness profile $\Sigma(r)$ of the stellar cluster. In all our isolated models, the change in the central surface brightness was negligible after 10 Gyr of evolution (with the only exception of model B1, where the change was -0.4 dex). The radius corresponding to the outmost reliable Draco isodensity contour of Odenkirchen et al. (2001) with $\Sigma = 12,060 M_\odot \text{ kpc}^{-2}$ ($r = 0.85$ kpc initially) increased by mere 0.03–0.05 dex.

Unfortunately, we observed significant evolution in the velocity anisotropy profiles $\eta(r)$ in our isolated models, especially at the center of the halo. All our best-fitting stellar models have a strong radial anisotropy at the center (see Table 1). In our N -body simulations with live DM halos the stellar core becomes close to isotropic within the first gigayear, suggesting that the particle-particle interactions are not the main culprit, as such effects would take gigayears to manifest themselves. This became more apparent after we ran simulations for all our models from Table 1 with $N_* = 30,000$ stellar particles and *static* DM potential. In this setup, close encounters between particles are extremely rare due to very low stellar density. In the static models we see the same effect (of slightly smaller magnitude) as in the runs with live DM halos: central radial anisotropy reduces almost to zero after a few crossing times. We do not know the exact reason for the above effect. The possible explanations are (1) the (unknown) DF corresponding to our choice of anisotropy, stellar density, and gravitational potential profiles is okay (positive everywhere), but the pseudo-Maxwellian approximation we use to set up the stellar velocities is not good for systems with strong radial anisotropy at the center, and/or (2) the DF is not physical (i.e., is negative) at the center. We also want to point out that a real stellar system cannot have a radial anisotropy all the way to its center, as the radial velocity dispersion diverges in such cases when $r \rightarrow 0$. To demonstrate this, we write down the solution of the Jeans equation (15) in the case of constant anisotropy (Łokas 2001),

$$\sigma_r^2 = \frac{1}{r^\zeta \rho_*} \int_r^\infty r'^\zeta \rho_* \frac{d\Phi}{dr} dr', \quad (24)$$

where the constant $\zeta \equiv 2\beta = 4\eta/(1 + \eta)$ is positive for the case of radial anisotropy. The integral in equation (24) is nonzero for $r = 0$, resulting in divergent σ_r at the center of the system. Obviously, in a real object, radial anisotropy should break down at some radius, changing into isotropy or tangential anisotropy. It is also hard to expect radially divergent velocity dispersion in a stellar system with a flat core, especially in the case of a flat-cored (Burkert) DM halo.

We want to emphasize that even though we cannot guarantee that the stellar models in Table 1 are physical (especially at the center), in our simulations they quickly relax to a stable configuration, with the surface brightness profile virtually identical to the observed one, and the line-of-sight velocity dispersion profile $\sigma_{\text{los}}(r)$ still consistent with the observations. In Figure 8 we plot $\sigma_{\text{los}}(r)$ profiles for our stellar models in a static DM potential after 10 Gyr of evolution integrated over the same six radial bins as the observational data of Wilkinson et al. (2004). As one can see, the profiles for evolved stellar clusters are a reasonably

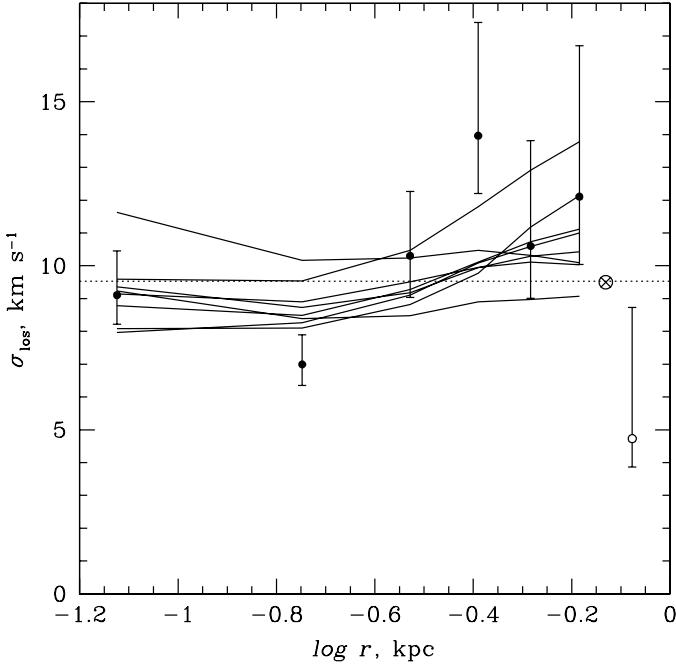


FIG. 8.—Line-of-sight stellar velocity dispersion profiles for Draco for the models evolved in a static DM halo potential. The notations are the same as in Fig. 3.

good match to the observations. (The χ^2 measure becomes a factor of 2 larger in the evolved models.)

We also used the isolated runs to estimate the accumulated total energy errors in our models. In the case of live DM halos, the total energy for DM + stars is conserved to better than $\sim 0.1\%$ (typically $\sim 0.05\%$) after 10 Gyr of evolution. To estimate the total energy errors for stars only, we measured the difference in stellar total energy at $t \sim 3$ Gyr (when the cluster has reached a steady state configuration) and at $t = 10$ Gyr in our static DM halo simulations. The difference was again $\lesssim 0.1\%$.

4.3. Tidal Stripping Simulations

We simulated evolution of the eight stars + DM models of Draco from Table 1 orbiting for 10 Gyr in the static spherically symmetric potential of the Milky Way given by equation (19). To run the simulations, we used the parallel version of the multi-stepping tree code Gadget (Springel et al. 2001). The number of stellar and DM particles and the corresponding gravitational softening lengths were the same as in the isolated models described in § 4.2. Each Draco model was simulated for six different orbits from Table 2. Initially, Draco was located at the apocenter of its orbit. Altogether we made 48 tidal stripping simulations. We refer to the models by both the model number from Table 1 and the orbit number from Table 2, e.g., model N1-5. Most of the results we give below are for the latest moment of time when the dwarf was located at the current distance of Draco from the Galactic center of ~ 82 kpc (we do not make distinction between the dwarf moving inward or outward), which took place 7.4–10 Gyr from the beginning of the simulations (9.4–10 Gyr for orbits 3–6).

All our models experienced tidal stripping of different degree. As Figure 9a shows, the DM mass of the gravitationally bound remnant is between 90% (model N5-1) and 0.1% (model N1-6) of the original mass at the end of the simulations. Three of our models became completely gravitationally unbound within 10 Gyr: B1-6 (after 3.2 Gyr and three pericenter passages), B2-6

(after 7.8 Gyr and six pericenter passages), and B1-5 (after 9.4 Gyr and seven pericenter passages). In the latter case, the dwarf is still bound when it is located at ~ 82 kpc at the end of the simulations (when we compare the results of the simulations with the observed properties of Draco)—but only barely so. It is not surprising that all the unbound models have Burkert halos. Indeed, for given mass and scaling radius, these halos have lower averaged density than NFW halos in the central area. If truncated instantaneously at a certain radius, the total energy of the remnant becomes positive for Burkert halos at a radius ~ 2.1 times larger than for NFW halos (Mashchenko & Sills 2005b).

Another result that can be explained is that the most massive halos are easier to strip and disrupt tidally than the less massive ones. All our models (both massive and of lower mass) have a comparable DM density within the observed extent of Draco (because of the virial theorem), so in the point mass approximation they should be equally susceptible to tidal forces. However, the point mass approximation (used to derive equation [23]) breaks down for our most massive halos, as their size becomes comparable to the pericentric distance, so the strongly nonlinear components of the tidal force become important. Not surprisingly, our most massive halos on orbit 6 were either totally disrupted (model B1-6) or lost 99.9% of its original mass (model N1-6) after 10 Gyr of evolution.

In all of our models a fraction of stars has been tidally stripped by the end of the simulations—even for orbit 1. In two cases (models B1-6 and B2-6), stars have become completely unbound by the time the dwarf was passing at the distance of ~ 82 kpc from the Galactic center for the last time. In other cases, the fraction of escaped stars was between $\sim 10^{-4}$ for models B1-2, B1-3, and B1-4, and 96.6% for model N1-6 (see Fig. 9b).

When analyzing the global properties of the stellar cluster at the end of the simulations, the most obvious result is the fact that the more disruptive the orbit is, the more the system is affected by the tidal shocks experienced near the pericenter of the orbit. (Orbits with a larger number from Table 2 are more disruptive for two reasons: they have smaller pericentric distance, and they have shorter orbital period, so the number of pericentric passages in 10 Gyr is larger.) Dwarfs are puffed up by the tidal shocks, with the central line-of-sight velocity dispersion σ_0 becoming smaller (Fig. 9c), central surface brightness decreasing (not shown, but is qualitatively similar to σ_0 behavior), and the projected half-light radius becoming larger (except for the extreme case of orbit 6, when both tidal shocking and tidal stripping are important; see Fig. 9d).

Our models are highly idealized when it comes to long-term evolution of stellar tidal streams. On our most disruptive orbits, 5 and 6, a significant fraction of stars become unbound over the course of the tidal evolution, with the most of the tidally stripped stars following very closely the almost radial orbit of the dwarf. From the Sun location, many of these stars project on a rather small area in the sky inside or around the apparent location of the dwarf. This can be quite unphysical, as such cold tidal streams are not expected to survive for many gigayears in the Milky Way halo due to its triaxiality and clumpiness (as predicted by cosmology) and due to interaction with baryonic structures in the Galaxy (stellar disk with spiral arms, stellar bar, giant molecular clouds). To circumvent this difficulty, in this section we discuss all the observable model properties for two extreme cases: (1) all stars are taken into account, and (2) only the stars (both bound and unbound) located within the spatial distance of 5 kpc from the center of the dwarf are considered. In the latter case, the spatial truncation of the tidal stream ensures

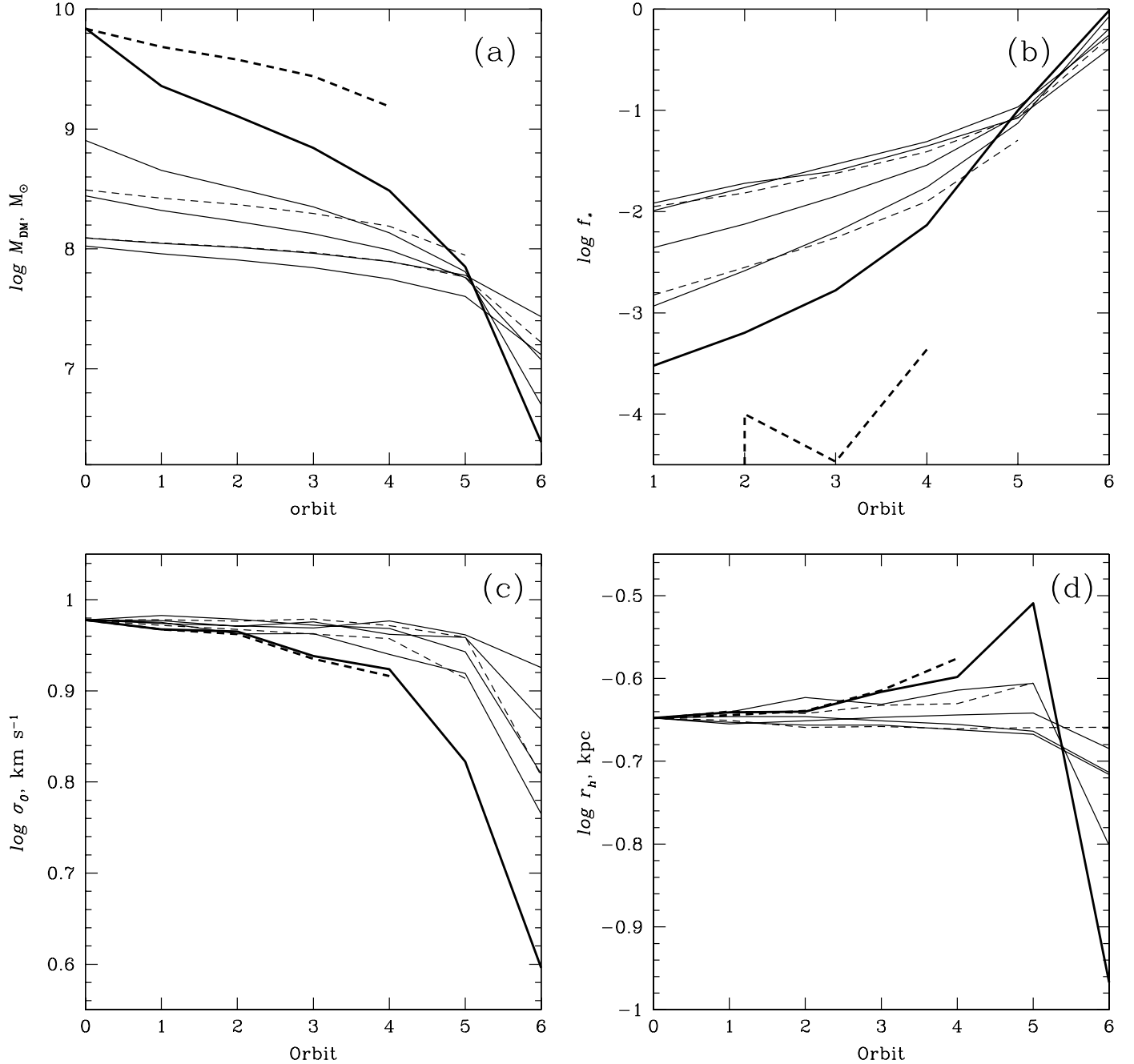


FIG. 9.—Draco models' parameters near the end of the simulations (when the dwarf was ~ 82 kpc away from the Galactic center) as a function of orbit. Solid/dashed lines correspond to models with NFW/Burkert DM halo profiles, respectively. Thick lines correspond to the most massive halos (models N1 and B1). (a) Gravitationally bound DM mass M_{DM} . (b) Fraction of stars having become unbound f_* . (c) Central line-of-sight stellar velocity dispersion σ_0 . (d) Projected half-light radius for the bound stellar cluster r_h . To facilitate the comparison of different models, both σ_0 and r_h are normalized to the same value for orbit 0 (corresponding to isolated models).

that only the most recently stripped stars are used for calculating the observable properties of the models.

On a more detailed level, the impact of both tidal shocks and tidal stripping and heating can be seen in Figure 10. Here we show the surface brightness profiles (Fig. 10a) and line-of-sight velocity dispersion profiles (Fig. 10b) for models N1-1, N1-4, N1-5, and N1-6. The most obvious effect in Figure 10 is the global decrease of σ_{los} for orbits with smaller pericentric distance (excluding orbit 6), accompanied by a small decrease in the central surface brightness and a slight radial expansion of the system. No obvious tidal truncation and tidal heating is observed in the outskirts in the cluster. These results were obtained for the stars located within the spatial distance of 5 kpc from the

center of the dwarf, but in the case when all stars are included the profiles are practically the same. Orbit 6 is a completely different case: one can see the σ_{los} being dramatically inflated in the outskirts of the dwarf due to superposition of tidally removed stars on the dwarf (Fig. 10b). This effect becomes even more dramatic when we include all the stars, with the line-of-sight velocity dispersion reaching 50–70 km s^{-1} in the outermost observed bin. As we discussed in the previous paragraph, it is quite unlikely that old tidal streams can stay so well collimated for many gigayears to produce the above effect. But even for the conservative case of considering only freshly stripped stars, the steeply growing σ_{los} profile for model N1-6 is grossly inconsistent with the observed profiles of Draco and other dwarf spheroidals,

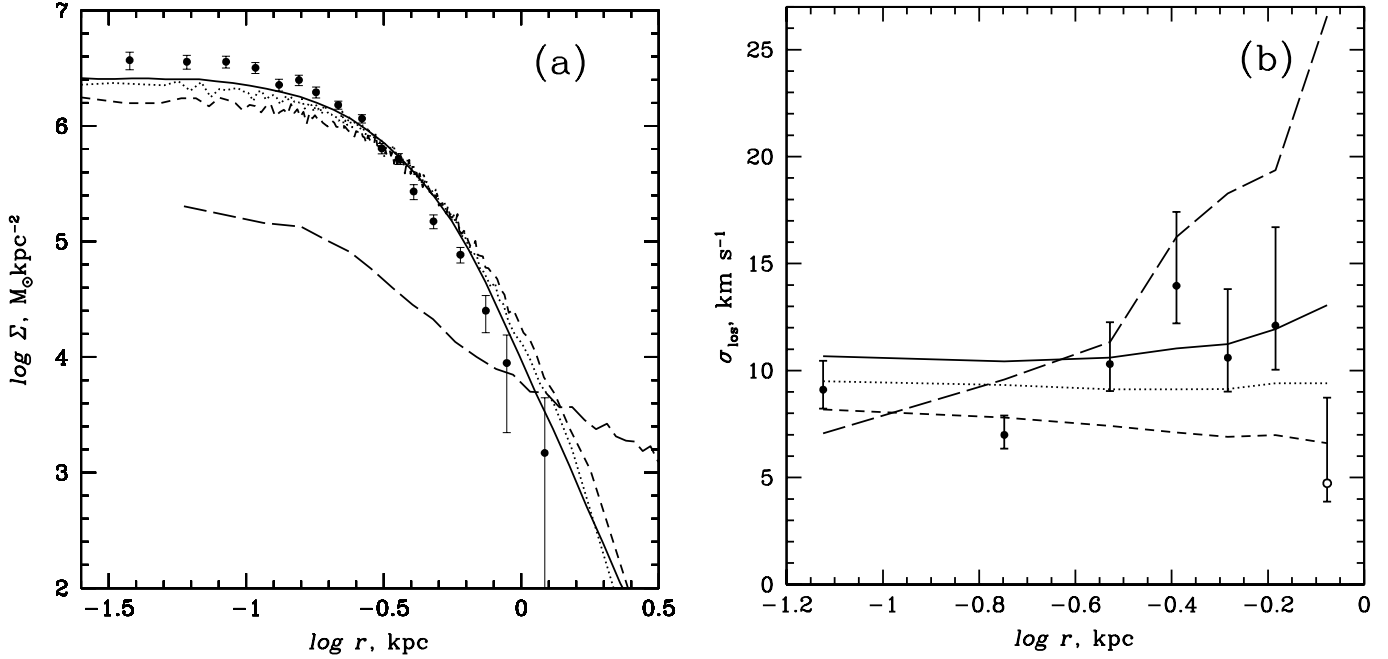


FIG. 10.—Observable properties of model N1 for a few different orbits near the end of the simulations (when the dwarf was ~ 82 kpc away from the Galactic center). Only stars (both bound and unbound) located within the spatial distance of 5 kpc from the dwarf’s center are considered. Solid, dotted, short-dashed, and long-dashed lines correspond to orbits 1, 4, 5, and 6, respectively. The observer is assumed to be located at the Galactic center. (a) Surface brightness profile $\Sigma(r)$. We also show the observed Draco profile of Odenkirchen et al. (2001, their sample S2). (b) Stellar line-of-sight velocity dispersion profile $\sigma_{\text{los}}(r)$. We also show the observed Draco velocities of Wilkinson et al. (2004).

where σ_{los} is either not changing or decreasing at large distances from the center.

The change in the surface brightness profile for model N1-6 is also quite dramatic (Fig. 10a, *long-dashed line*). The outer $\Sigma(r)$ slope becomes very shallow, which is inconsistent with the observed profiles for Galactic dSphs. The slope becomes even more shallow when we include stars beyond the spatial distance of 5 kpc from the center of the dwarf. Similar behavior (in terms of shallow outer Σ profiles and inflated σ_{los} in the outskirts of the dwarf) is also observed in other models with orbit 6 (both bound and unbound). The possible exceptions are models N4-6 and N5-6, which are consistent with the observations of Draco when we consider only freshly stripped stars. We conclude that it is unlikely that Draco and other Galactic dSphs have experienced tidal interactions as dramatic as our models on orbit 6.

To facilitate the comparison of our models with the observed stellar isodensity contours of Draco of Odenkirchen et al. (2001), we designed the following projection algorithm. (1) The frame of reference is rotated to place the center of the dwarf on the negative side of axis Z , with axis X located in the orbital plane of the dwarf and pointing in the direction of the orbital motion. (2) As the direction of the proper motion of Draco is not known (see discussion in § 4.1) and the current angle between the vector connecting Draco with the center of the Galaxy and the vector connecting Draco with Sun is $\varphi = 5^\circ 7'$, we consider three extreme cases of the possible vantage point location that should encompass the whole range of projected model appearances: the view from the Galactic center ($\varphi = 0^\circ$), the view from a point in the orbital plane of Draco located at 82 kpc from the dwarf with $\varphi = 5^\circ 7'$, and the view from a point in the plane that is perpendicular to the orbital plane of Draco at 82 kpc and with $\varphi = 5^\circ 7'$. We found that due to the fact that for Draco the angle φ is small (which is also the case for other Galactic dSphs, with the exception of Sagittarius), the observable properties of our models (Σ and σ_{los} profiles and surface brightness maps) do not depend

noticeably on the vantage point we choose—especially for the case when we only include freshly stripped stars. (3) We exclude stars with $z > -8.5$ kpc to avoid contamination of our maps with local tidal stream overdensities that would be discarded by observers as local Galactic stars. (4) We perform prospective projection of the stellar particles smoothed with a Gaussian beam that has a fixed physical size (either 0.15 or 0.5 kpc) and brightness inversely proportional to the square of the distance of the particle from the observer. This procedure makes the “surface brightness” of individual particles invariant of the distance from the observer, which is appropriate for spatially resolved clumps of the tidal stream.

The most interesting result obtained from the analysis of the surface brightness maps is the lack of the classical S-shaped tidal tails in our models. In the case of significant tidal stripping (Fig. 11, two different vantage points are shown) the stellar isodensity contours change from being spherical near the center of the dwarf to being increasingly more elliptical and often off-centered at larger distances. In the cases with less severe stripping, outer contour boxiness is observed in some of the models. For orbits 1–3 the surface density of the tidally removed stars is so low that it is hard to draw any conclusion as to the shape of the tidally distorted isodensity contours (except for the fact that the galaxy is observed against the background and/or foreground of a few degrees wide belt of tidally stripped stars). The explanation for the above effect is in the facts that the tidal stripping is significant only for very eccentric (almost radial) Draco orbits with $R_p \lesssim 20$ kpc, and that currently Draco is located $\gtrsim 10$ kpc away from the apocenter of its orbit (see Table 2). Under these circumstances, the line of sight practically coincides with the direction of the tidal elongation of Draco, with both tidal tails seen edge-on. This is an interesting result, as it suggests that the lack of S-shaped isodensity contours in the outskirts of the Galactic dSphs cannot be used to support a claim that the dwarf has not experienced significant tidal stripping in the gravitational

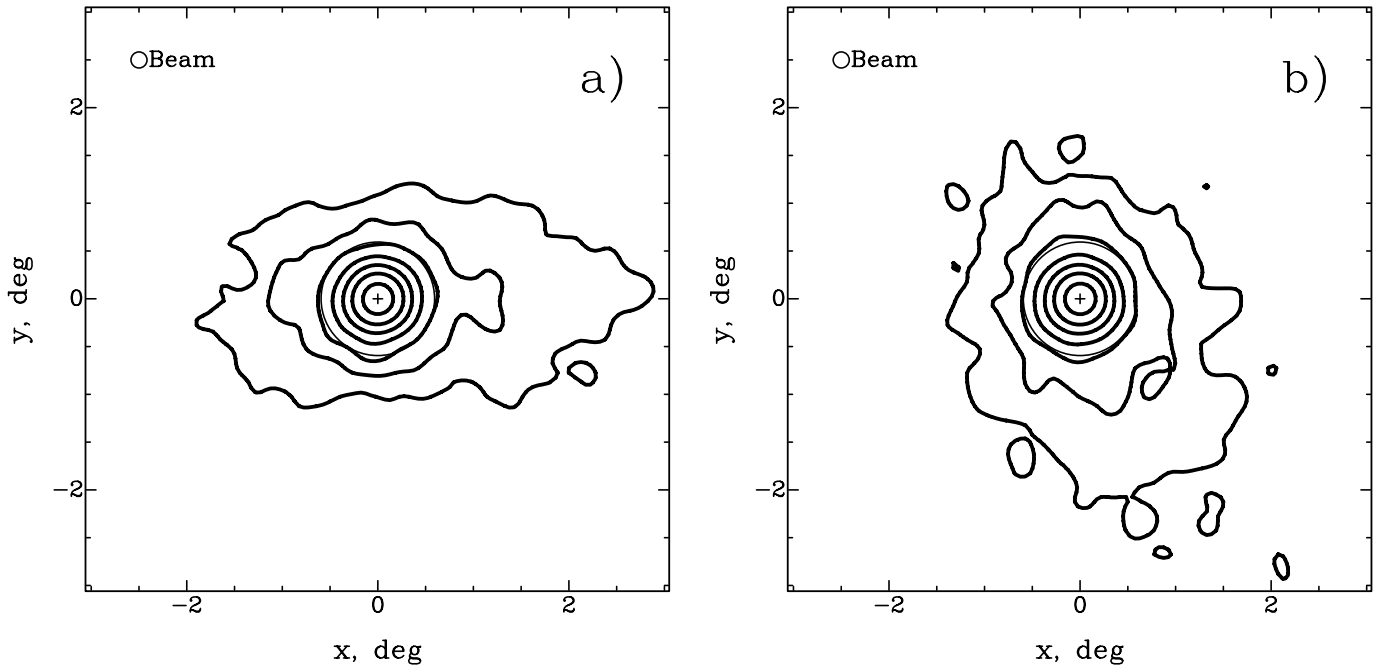


FIG. 11.—Stellar surface brightness maps for model N2-6 near the end of the simulations (when the dwarf was ~ 82 kpc away from the Galactic center). The contour levels are $(8, 16, 32, \dots, 512) \times 10^3 M_\odot \text{ deg}^{-2}$ (calculated for the nominal distance of Draco of 82 kpc). A cross marks the center of the dwarf. The thin-line circle has a radius of 0.85 kpc—the radius of the Draco 2σ surface brightness contour of Odenkirchen et al. (2001). In the top left corner we show the size of the Gaussian beam used to make the maps. (a) The observer is in the plane of the Draco's orbit. (b) The observer is in the plane perpendicular to the Draco's orbit.

potential of the Milky Way. It appears that the presence (absence) of tidally heated stars in the outskirts of dSphs is much more sensitive indicator of tidal stripping being significant (not significant).

We measured for all our models the critical surface brightness Σ_c when the outer isodensity contours become noticeably distorted due to tidal effects. The two models that became gravitationally unbound by the end of the simulations (B1-6 and B2-6) show very distorted contours all the way to the center of the dwarf (see Fig. 12). They also have dramatically inflated line-of-sight stellar velocity dispersion profiles (up to $50\text{--}100 \text{ km s}^{-1}$) and very shallow outer surface brightness slopes. All of the above makes these two models (and most probably any other unbound model for a dSph) completely inconsistent with the observed properties of the Galactic dSphs. Among the bound models, the one that has experienced the most dramatic tidal stripping (model N1-6) is also the one that has the largest value for Σ_c : $\sim 4 \times 10^4 M_\odot \text{ deg}^{-2}$, which would correspond to $\sim 3\sigma$ isodensity contour of Odenkirchen et al. (2001). In all other cases, the value of Σ_c is significantly lower: $(7.4\text{--}17) \times 10^3 M_\odot \text{ deg}^{-2}$ for the models of orbit 6, and less than $10^3 M_\odot \text{ deg}^{-2}$ for other orbits. For orbits 1, 2, and 3, Σ_c was too small to be measured. These values of Σ_c are significantly lower (by a factor of $\gtrsim 1.5$) than the 2σ detection limit of Odenkirchen et al. (2001). The angular radius of the smallest distorted isodensity contour is $\sim 1^\circ$ for orbit 6 (with the exception of models B1, B2, and N1) and $\gtrsim 1.8$ for other orbits.

One very interesting special case is that of model B1. This model has a halo with a flat DM core of size $r_s \sim 1.4$ kpc (see Table 1), so all the observed extent of Draco is within this large harmonic core. In Figure 13 we show the inner (corresponding to the observed part of Draco) isodensity contours for models B1-4 and B1-1. Unlike all other models (both NFW and Burkert), here one can see a relatively strong tidal distortion of the contours at distances $\lesssim 0.5$ from the center of the dwarf. The distortions are substantial even for orbit 1 (Fig. 13b), which has the largest pericentric distance of 70 kpc. The distorted contours are

both elliptical and nonconcentric. Interestingly, the effect is minimal for the two orbits that have the smallest eccentricity—orbits 2 and 3 with $R_a/R_p \lesssim 2.6$. The distortions are strong for the more eccentric orbits 1, 4, and 5. It appears that it is the variability of the tidal force rather than its strength that is the primary governing factor for the above effect. As the observed stellar isodensity contours of Draco are very regular and concentric (Odenkirchen et al. 2001), results of our simulations suggest that it is unlikely that Draco resides in a large DM harmonic core—unless it happened to move on a close to circular orbit with $R_p \sim 45\text{--}65$ kpc and $R_a/R_p \lesssim 2.6$.

5. DISCUSSION

In this paper we presented a sequence of composite (stars + DM) models for Draco, listed in Table 1, which satisfy all the available observational and cosmological constraints. We showed that for the most of physically plausible orbits of Draco in the Galactic potential the tidal forces could not modify the observable properties of our models appreciably after 10 Gyr of evolution. Both “standard” cuspy NFW DM halos and Burkert halos with a flat core provide a reasonably good description of Draco. The properties of a Burkert halo are better constrained by our analysis. Most importantly, if Draco has a flat core, it should have formed at or before the end of the reionization of the universe: $z \gtrsim 6.5$. Tidal stripping simulations put even stronger constraints on the flat-core case: we showed in the previous section that our most massive Burkert model, B1, would be consistent with the observations only for a very limited range of possible Draco orbits: orbit 6 is ruled out as the model becomes completely unbound with dramatically inflated σ_{los} and very shallow Σ profiles, whereas for orbits 1, 4, and 5 (and also 6) we observe significant distortion of inner stellar isodensity contours that is most definitely not consistent with the regular isodensity contour shape observed in Draco by Odenkirchen et al. (2001). Only the lowest eccentricity orbits, 2 and 3, are not ruled out by our analysis.

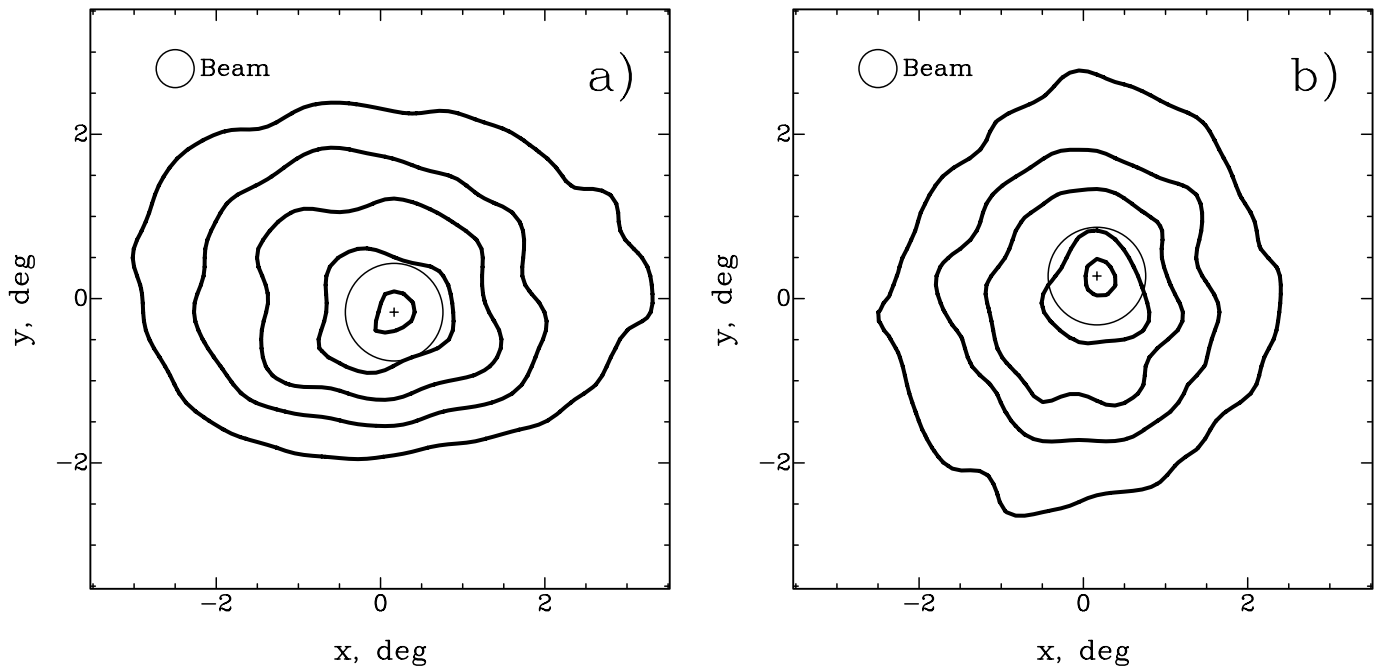


FIG. 12.—Surface brightness maps for the two unbound models at the end of the simulations (when the dwarf is located at $R \sim 82$ kpc). Only freshly stripped stars (within a radius of 5 kpc from the dwarf) are included. The observer is located at the center of the Galaxy. A cross marks the center of the dwarf. In the top left corner we show the size of the Gaussian beam used to make the maps. (a) Model B1-6. Contours are $(4-19) \times 10^3 M_{\odot} \text{ deg}^{-2}$. (b) Model B2-6. Contours are $(1-8.6) \times 10^3 M_{\odot} \text{ deg}^{-2}$.

An NFW halo is less constrained by the available observations of Draco: the halo formation redshift z is anywhere between ~ 2 and ~ 10 , whereas the initial virial mass could be between $\sim 10^8$ and $\sim 5 \times 10^9 M_{\odot}$. In the smaller mass (and larger z) limit the halos are so sturdy that even for our most disruptive orbit 6 the observable parameters of the model can still be consistent with the Draco observations after 10 Gyr of tidal evolution. If Draco was accreted by the Milky Way more recently than 10 Gyr ago, the impact of the tidal forces would be even smaller. For more massive NFW halos and for all Burkert models orbit 6 can be ruled out as the model predicts inflated line-of-sight velocity

dispersion in the outskirts of the dwarf, which would be at odds with observations.

How strong is our case against Draco (and other dSphs) being a “tidal dwarf”—remnants of a dwarf galaxy that are not gravitationally bound at the present time? In the previous section we suggested that the fact that the line-of-sight velocity dispersion is dramatically (by up to an order of magnitude) inflated in our two “tidal dwarf” candidates, models B1-6 and B2-6, can be used to rule out the “tidal dwarf” explanation for Draco. Here we want to caution that a more detailed comparison between the model and observations is required to critically assess our conclusion.

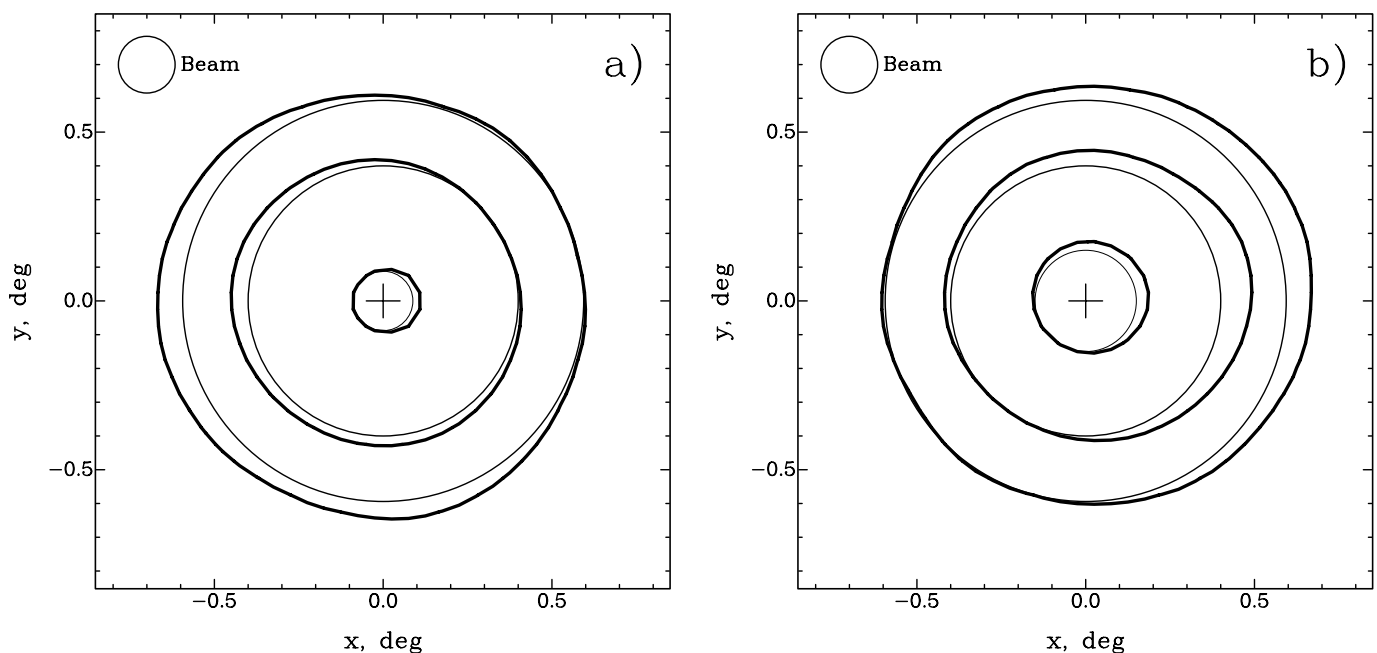


FIG. 13.—Stellar surface brightness maps for the B1 models near the end of the simulations (when the dwarf was ~ 82 kpc away from the Galactic center). A cross marks the center of the dwarf. In the top left corner we show the size of the Gaussian beam used to make the maps. (a) Model B1-4. (b) Model B1-1.

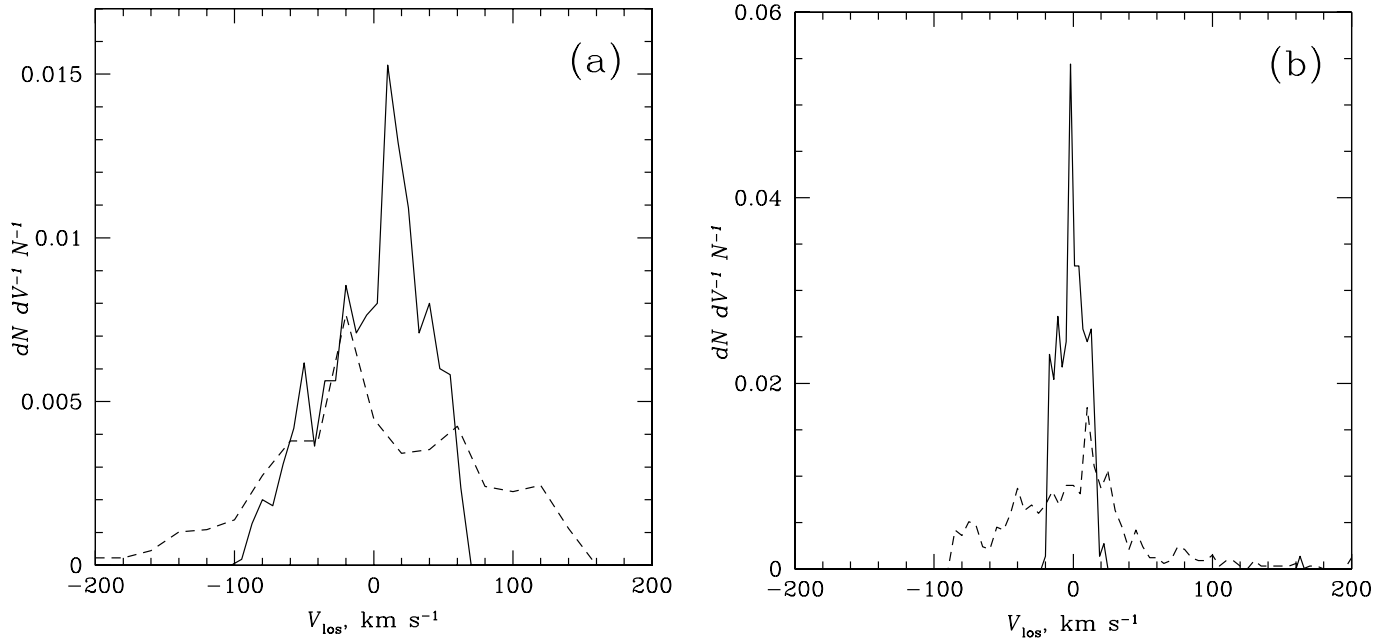


FIG. 14.—Distribution of line-of-sight velocities V_{los} for the models that became unbound by the end of the simulations. The observer is located at the center of the Galaxy. The dwarf is located ~ 82 kpc away from the center of the Galaxy. Solid and dashed lines correspond to the stars within the spatial distance of 5 and 30 kpc from the densest part of the unbound dwarf, respectively. Only stars located within 0.5° from the densest part of the galaxy are taken into account. (a) Model B1-6. (b) Model B2-6.

Our large estimates of σ_{los} were derived for stars with any line-of-sight velocity projected onto the dwarf disk and optionally restricted to lie within the spatial distance of 5 kpc from the dwarf's center. Many of the high-velocity tidal tail stars responsible for inflating σ_{los} would be discarded by observers as “not belonging to the galaxy.” In Figure 14 we show the distribution of line-of-sight velocities V_{los} for models B1-6 and B2-6. We show separately histograms for freshly stripped stars (*solid lines*) and for all stars projected on the disk of the dwarf (*dashed lines*). As one can see, the situation depends strongly on how recently the dwarf became unbound, and on the longevity of the cold tidal streams in the Galactic halo. Model B1-6 became unbound many orbits (almost 7 Gyr) ago and has a very wide distribution of V_{los} —even for freshly stripped stars. Model B2-6, on the other hand, became unbound only ~ 2 Gyr ago, and has more complex distribution of V_{los} . In this model, the freshly removed stars are virtually all concentrated within a relatively narrow interval, with σ_{los} being inflated mainly due to the presence of one high-velocity stellar particle with $V_{\text{los}} \simeq 160 \text{ km s}^{-1}$. Such stars will definitely be discarded by observers. When we consider all stars (Fig. 14b, *dashed line*), the distribution of V_{los} is much wider than in Galactic dSphs. In the case of model B2-6, the situation thus sensitively depends on how long the tidal stream can stay collimated in the Milky Way potential.

Another important evidence against Draco being an unbound stream of stars is presented in Figure 12. Here we show surface brightness maps for our two unbound models, B1-6 and B2-6. One can see that the contours are irregular and not concentric—even near the center of the dwarf. This is in sharp contrast with the regular appearance of the observed isodensity contours in Draco (Odenkirchen et al. 2001).

Pending the arrival of accurate proper motion measurements for Draco, let us be slightly more definitive in trying to determine the nature and cosmological significance of Draco by assuming that it is moving on orbit 3, which is the most probable one (see § 4.1). From Figure 9 one can then infer that if Draco is a cosmological halo, its current DM mass is between 7×10^7 and $3 \times 10^9 M_\odot$, the fraction of the tidally stripped stars is $< 3\%$, and

the central line-of-sight velocity dispersion σ_0 , central surface brightness Σ_0 , and the half-light radius r_h have changed due to tidal shocks by no more than -0.07 , -0.04 , and 0.03 dex, respectively, in the last 10 Gyr. This orbit has $R_p = 51.1$ kpc, placing it well outside of the Galactic disk. Stellar tidal tails produced by our models on this orbit are extremely weak, with the surface brightness sensitivity required to see the isodensity contours distorted due to tidal forces being better than $\sim 200 M_\odot \text{ deg}^{-2}$, or more that 2 orders of magnitude better than the observations of Odenkirchen et al. (2001). The DM halo could be either NFW or Burkert, and was formed after $z \sim 11$. Our results then support either of the two recently proposed solutions to the “missing satellites” problem (Klypin et al. 1999; Moore et al. 1999): that the Galactic dSphs are the most massive subhalos predicted by cosmological simulations to orbit in the halo of a Milky Way-sized galaxy (Stoehr et al. 2002; Hayashi et al. 2003), or that the Galactic dSphs are the halos that managed to form stars before the reionization of the universe was completed around $z \sim 6.5$ (Bullock et al. 2000). Our analysis suggests that unfortunately there are not enough observational data yet to discriminate between the two above scenarios. Much better quality line-of-sight velocity dispersion profiles, deeper surface brightness maps, and ideally accurate proper motion measurements are required to produce further progress in this direction.

We would like to mention a few most important deficiencies of our tidal stripping model. The first one is due to our use of a spherically symmetric potential for the Milky Way. As a result, we ignore disk shocking, which can be very important for the orbits with $R_p \lesssim 20$ kpc. We tried to partly circumvent this deficiency by considering an orbit with extremely small pericentric distance: orbit 6, with $R_p \simeq 2.5$ kpc. Ideally, we would prefer to include the disk in our simulations, but this would result in significant increase in number of required models, which would make our project not feasible with the current level of computing power.

The second problem is generic to existing tidal stripping simulations of Galactic satellites (dSphs and globular clusters), and is caused by our use of a static potential for the Milky Way

halo. In a realistic (live) Galactic halo very massive satellites should experience dynamical friction, which would gradually bring them closer to the center of the Galaxy. Unfortunately, we could not use a simple analytical formula to estimate the impact of the dynamical friction on our results. The dynamical friction would be strongest for orbits 6 and 5, which have the smallest pericentric distances. Our subhalos on these orbits experience dramatic mass loss (up to 90% and 70%, respectively) during the first pericentric passage, rendering the constant satellite mass formula of Binney & Tremaine (1987) not applicable. The dynamical friction equation of Colpi et al. (1999) does not have this limitation, but it was derived for the special case of a subhalo with a truncated isothermal DM density profile with a core that is very different from both the NFW and Burkert profiles of our subhalos. We want to emphasize that the inclusion of dynamical friction in our model would make our conclusion, that the observable properties of the most of our dwarfs were not affected noticeably by tidal forces, even stronger, as the dwarfs would start off at larger distance from the Milky Way center where the tidal forces are weaker.

In addition, the use of static potential ignores the impact of the gravitational field of the satellite on the Milky Way halo. This effect can be very important for massive dwarfs on almost radial orbits, with the potential of both the satellite and the Milky Way center violently fluctuating during the pericentric passage, leading to an exchange of energy between the dwarf and the Galactic halo (similar to the mechanism of violent relaxation). The above effect would probably be important only for orbit 6, which we were able to rule out for most of our Draco models.

It is important to mention that our models do not cover all possible initial configurations of Draco. In a more general case, one would have to start with arbitrary initial stellar and DM density profiles (with the initial stellar velocity dispersion profile following from eq. [6]). After 10 Gyr of evolution in the Galactic tidal field both profiles could become substantially different, with the line-of-sight velocity dispersion either increasing (due to the projection of unbound stars) or decreasing (due to tidal shocks; see Fig. 10). The more general case would require a dramatic increase in supercomputing time, which would make our approach infeasible. We want to emphasize that despite the fact that our

models probably do not include all possible initial Draco configurations, they do constitute a family of fully self-consistent models that match well all the available observations of Draco.

A potentially important evolutionary factor not included in our model is an interaction between Draco and dark subhalos, predicted to be present in the Milky Way halo in large numbers by Λ CDM cosmological models. This effect was studied on larger scales by Moore et al. (1998), who showed that in a cluster environment the galaxy-galaxy harassment can be substantial. It is not clear whether the harassment on a smaller, galactic scale would be of the same order: unlike the cluster scale, where the numbers of modeled and observed galaxies are in good agreement, there is a “missing satellites” issue on galactic scales.

6. CONCLUSIONS

We presented two one-parameter families (separately for NFW and Burkert DM density profiles) of composite (stars + DM) models for Draco that satisfy all the available observational and cosmological constraints. We showed that these models can survive tidal shocks and stripping on most realistic Draco orbits in the Galactic potential for 10 Gyr, with no appreciable impact on their observable properties. Both NFW and Burkert DM halo profiles are found to be equally plausible for Draco. The DM halos are either massive (up to $\sim 5 \times 10^9 M_\odot$) and recently formed ($z \sim 2-7$), or less massive (down to $\sim 7 \times 10^7 M_\odot$) and older ($z \sim 7-11$). Consequently, our results can be used to support either of the two popular solutions of the missing satellites problem—“very massive dwarfs” and “very old dwarfs.” Higher quality observations (line-of-sight velocity dispersion profiles, surface brightness maps, proper motion measurements) are required to further constrain the properties of Galactic dSphs and to place them in the right cosmological context.

We would like to thank Jan Kleyna for providing the observed line-of-sight velocity dispersion profile for Draco. The simulations reported in this paper were carried out on McKenzie cluster at the Canadian Institute for Theoretical Astrophysics.

APPENDIX

DERIVATION OF SPACE VELOCITY VECTOR COMPONENTS FOR GALACTIC SATELLITES

In this section we derive the components of the space velocity vector of an object with known distance from the Sun D , heliocentric line-of-sight velocity V_{los} , and two proper motion components $\mu_\alpha \cos \delta$ and μ_δ . We work with the frame of reference where the center is at the Sun, axis X is directed toward the Galactic center, axis Y is pointing at ($l = 90^\circ, b = 0$), and axis Z is directed toward the north Galactic pole ($b = 90^\circ$). Here (l, b) are the Galactic coordinates. The frame of reference is at rest relative to the Galactic center. The solar velocity vector in this frame of reference is $\mathbf{V}_\odot = \{10.0, 225.25, 7.17\} \text{ km s}^{-1}$ (Dehnen & Binney 1998). We assume that the Sun is located at the distance $R_\odot = 8.5 \text{ kpc}$ from the Galactic center.

To convert the proper motion vector components from equatorial to Galactic frame of reference, one can use

$$\mu_l \cos b = (\mu_\alpha \cos \delta) \cos \varphi - \mu_\delta \sin \varphi, \quad (\text{A1})$$

$$\mu_b = (\mu_\alpha \cos \delta) \sin \varphi + \mu_\delta \cos \varphi, \quad (\text{A2})$$

where the angle φ is obtained from

$$\cos \varphi = (\sin \delta_{\text{NGP}} - \sin \delta \sin b) / (\cos \delta \cos b), \quad (\text{A3})$$

$$\sin \varphi = -\sin(\alpha - \alpha_{\text{NGP}}) \cos \delta_{\text{NGP}} / \cos b. \quad (\text{A4})$$

Here (α, δ) and (l, b) are the equatorial and Galactic coordinates of the object, respectively, and ($\alpha_{\text{NGP}}, \delta_{\text{NGP}}$) are the equatorial coordinates of the north Galactic pole (for the J2000.0 equinox, $\alpha_{\text{NGP}} = 192^\circ 859$ and $\delta_{\text{NGP}} = 27^\circ 128$).

One can show that the three components of the space velocity vector of the object in the frame of reference moving with the Sun are

$$U_z = zV_{\text{los}} + D\mu_b(x^2 + y^2)^{1/2}, \quad (\text{A5})$$

$$U_x = [x(V_{\text{los}} - zU_z) - D(\mu_l \cos b)y(x^2 + y^2)^{1/2}]/(x^2 + y^2), \quad (\text{A6})$$

$$U_y = [D(\mu_l \cos b)(x^2 + y^2)^{1/2} + yU_x]/x, \quad (\text{A7})$$

where $x = \cos l \cos b$, $y = \sin l \cos b$, and $z = \sin b$ are the components of a unit vector directed from the Sun toward the object, and the units for D , U , and the two proper motion components ($\mu_l \cos b$, μ_b) are km, km s⁻¹, and rad s⁻¹, respectively.

In the frame of reference that is at rest relative to the Galactic center, the space velocity vector of the object is $\mathbf{V} = \mathbf{U} + \mathbf{V}_\odot$. In the cylindrical Galactic frame of reference, the three components of the space velocity vector of the object are

$$\Pi = (S_x V_x + S_y V_y)/(S_x^2 + S_y^2)^{1/2}, \quad \Theta = (S_y V_x - S_x V_y)/(S_x^2 + S_y^2)^{1/2}, \quad W = V_z, \quad (\text{A8})$$

where Π is directed outward from the Galactic center in the plane of the Galaxy, Θ is the circular rotation speed in the plane of the Galaxy (positive for the Sun), W is directed toward the north Galactic pole, and $\mathbf{S} = \{xD - R_\odot, yD, zD\}$ is the vector connecting the Galactic center with the object. In the spherical Galactic frame of reference, the radial and tangential velocities of the object are

$$V_r = (\mathbf{V} \cdot \mathbf{S})/|\mathbf{S}|, \quad V_t = (|\mathbf{V}|^2 - V_r^2)^{1/2}. \quad (\text{A9})$$

REFERENCES

- Aaronson, M. 1983, *ApJ*, 266, L11
 Battaglia, G., et al. 2005, *MNRAS*, 364, 433
 Binney, J., & Tremaine, S. 1987, *Galactic Dynamics* (Princeton: Princeton Univ. Press)
 Bullock, J. S., Kolatt, T. S., Sigad, Y., Somerville, R. S., Kravtsov, A. V., Klypin, A. A., Primack, J. R., & Dekel, A. 2001, *MNRAS*, 321, 559
 Bullock, J. S., Kravtsov, A. V., & Weinberg, D. H. 2000, *ApJ*, 539, 517
 Burkert, A. 1995, *ApJ*, 447, L25
 Cardone, V. F., & Sereno, M. 2005, *A&A*, 438, 545
 Colpi, M., Mayer, L., & Governato, F. 1999, *ApJ*, 525, 720
 Dehnen, W., & Binney, J. J. 1998, *MNRAS*, 298, 387
 Hayashi, E., Navarro, J. F., Taylor, J. E., Stadel, J., & Quinn, T. 2003, *ApJ*, 584, 541
 Hernquist, L. 1990, *ApJ*, 356, 359
 Johnston, K. V., Sigurdsson, S., & Hernquist, L. 1999, *MNRAS*, 302, 771
 Kazantzidis, S., Magorrian, J., & Moore, B. 2004, *ApJ*, 601, 37
 King, I. R. 1966, *AJ*, 71, 64
 Klessen, R. S., Grebel, E. K., & Harbeck, D. 2003, *ApJ*, 589, 798
 Klypin, A., Kravtsov, A. V., Valenzuela, O., & Prada, F. 1999, *ApJ*, 522, 82
 Klypin, A., Zhao, H., & Somerville, R. S. 2002, *ApJ*, 573, 597
 Kroupa, P. 1997, *NewA*, 2, 139
 Łokas, E. L. 2001, *MNRAS*, 327, L21
 Mashchenko, S., Carignan, C., & Bouchard, A. 2004, *MNRAS*, 352, 168
 Mashchenko, S., Couchman, H. M. P., & Sills, A. 2005, *ApJ*, 624, 726
 Mashchenko, S., & Sills, A. 2005a, *ApJ*, 619, 243
 ———. 2005b, *ApJ*, 619, 258
 Mateo, M. L. 1998, *ARA&A*, 36, 435
 Mateo, M. L., Olszewski, E. W., Vogt, S. S., & Keane, M. J. 1998, *AJ*, 116, 2315
 Merritt, D. 1985, *AJ*, 90, 1027
 Miyamoto, M., & Nagai, R. 1975, *PASJ*, 27, 533
 Moore, B., Ghigna, S., Governato, F., Lake, G., Quinn, T., Stadel, J., & Tozzi, P. 1999, *ApJ*, 524, L19
 Moore, B., Lake, G., & Katz, N. 1998, *ApJ*, 495, 139
 Munoz, R. R., et al. 2005, *ApJ*, 631, L137
 Navarro, J. F., Frenk, C. S., & White, S. D. M. 1997, *ApJ*, 490, 493
 Odenkirchen, M., et al. 2001, *AJ*, 122, 2538
 Oh, K. S., Lin, D. N. C., & Aarseth, S. J. 1995, *ApJ*, 442, 142
 Osipkov, L. P. 1979, *Pis'ma Astron. Zh.*, 5, 77
 Piatek, S., & Pryor, C. 1995, *AJ*, 109, 1071
 Piatek, S., Pryor, C., Bristow, P., Olszewski, E. W., Harris, H. C., Mateo, M., Minniti, D., & Tinney, C. G. 2005, *AJ*, 130, 95
 Read, J. I., Wilkinson, M. I., Wyn Evans, N., Gilmore, G., & Kleyna, J. T. 2006, *MNRAS*, in press (astro-ph/0511759)
 Ricotti, M., & Gnedin, N. Y. 2005, *ApJ*, 629, 259
 Sakamoto, T., Chiba, M., & Beers, T. C. 2003, *A&A*, 397, 899
 Scholz, R.-D., & Irwin, M. J. 1994, in *IAU Symp. 161, Astronomy from Wide-Field Imaging*, ed. H. T. MacGillivray (Dordrecht: Kluwer), 535
 Sheth, R. K., & Tormen, G. 1999, *MNRAS*, 308, 119
 Spergel, D. N., et al. 2003, *ApJS*, 148, 175
 Springel, V., Yoshida, N., & White, S. D. M. 2001, *NewA*, 6, 79
 Sternberg, A., McKee, C. F., & Wolfire, M. G. 2002, *ApJS*, 143, 419
 Stoeck, F., White, S. D. M., Tormen, G., & Springel, V. 2002, *MNRAS*, 335, L84
 van Albada, T. S. 1982, *MNRAS*, 201, 939
 Wilkinson, M. I., Kleyna, J. T., Evans, N. W., Gilmore, G. F., Irwin, M. J., & Grebel, E. K. 2004, *ApJ*, 611, L21